scientific reports

OPEN

Multiscale characterization of micro fracture connectivity and gas migration in volcanic reservoirs using µCT and hybrid learning segmentation

Jiacheng Zhang, Yunliang Yu✉, Hongchen Cai, Mengyu Li & Yingchun Liu

Volcanic reservoirs contain highly heterogeneous and extremely tight pore and fracture systems that exert a primary control on natural gas storage and migration. Accurate identification of micro fractures in µCT images remains challenging because fracture apertures are small, morphologies are complex, and grayscale contrast is low. To address this issue, this study develops an integrated framework that combines ensemble learning with a 2.5D deep learning model to achieve efficient and precise segmentation of volcanic micro fractures. A Random Forest model is first used to provide rapid pre segmentation, followed by a U Net plus plus model that captures through plane continuity and improves fracture boundary recognition. A semi-automatic label as you train strategy reduces annotation requirements while maintaining high accuracy. The model achieves a Dice coefficient of 0.902 within ten epochs. Based on the segmentation results, three dimensional reconstruction, pore throat network modeling and gas flow simulations were conducted to quantify fracture connectivity and reveal gas migration behavior. The results show that highly connected fractures create axial flow channels and lateral micro pathways that enhance seepage efficiency and govern the overall migration process of natural gas. Samples with larger pore throat radii and stronger multiscale connectivity present significantly higher permeabilities and more continuous flow paths. This study provides a practical and accurate fracture segmentation workflow and quantitatively demonstrates how micro fracture connectivity regulates gas transport in tight volcanic reservoirs. The findings offer theoretical and methodological support for digital rock analysis, reservoir evaluation and multiscale modeling in geomechanics.

Keywords Volcanic reservoir, Digital rock, 3D modeling, Deep learning, Ensemble learning, Gas migration

Abbreviations

LPA	Low-pressure gas adsorption
MIP	Mercury intrusion porosimetry
NMR	Nuclear magnetic resonance
SANS	Small-angle neutron scattering
µCT	Micro-computed tomography
PNM	Pore network modeling
EIA	Environmental impact assessment
FOV	Field of view
REV	Representative fundamental volume

With the global energy structure shifting toward low-carbon and diversification, unconventional oil and gas resources are becoming increasingly important for ensuring energy security and promoting economic development[1]. Among various unconventional reservoirs, volcanic reservoirs are widely distributed and have complex lithofacies; their storage space is mainly composed of pores, micro-fractures, and dissolution features[2,3]. The micro-fracture system, in particular, exerts a first-order control over reservoir connectivity and the efficiency

College of Earth Sciences, Jilin University, Changchun 130061, China. ✉email: yuyunliang@jlu.edu.cn

of hydrocarbon migration and production[4]. The geometric architecture and topological connectivity of the micro-fracture system impose direct constraints on fluid transmissibility, serving as a core metric for evaluating reservoir connectivity and predicting production performance[5]. Nevertheless, a systematic understanding of the structural characteristics of micro-fractures in volcanic reservoirs and their quantitative impacts on migration behavior remains lacking.

Conventional methods such as low-pressure gas adsorption (LPA), mercury intrusion porosimetry (MIP), nuclear magnetic resonance (NMR), and small-angle neutron scattering (SANS) can reveal pore-scale features but are generally insufficient to directly characterize the 3D spatial morphology and connectivity of micro-fractures[6]. µCT imaging provides volumetric information, yet under low contrast, beam-hardening and ring artifacts, and sub-voxel effects, it is difficult to robustly delineate fracture boundaries, and traditional thresholding or filtering approaches may incur significant errors in fracture identification[7,8]. On the same time, the finite spatial resolution (voxel size) of CT imaging imposes inherent limitations on detecting sub-micron fractures. Therefore, how to leverage advanced intelligent image-segmentation algorithms to achieve high-precision recognition of micro-fractures has become a key bottleneck restricting research on volcanic reservoirs.

In recent years, rapid progress in artificial intelligence has created new opportunities for rock-image processing. Ensemble-learning algorithms such as random forests and support vector machines have been used to improve automatic recognition in 2D imagery[8]; deep learning represented by U-Net and its variants has demonstrated powerful feature-extraction capabilities in complex textures[9,10]. However, 3D networks often face high computational costs and prolonged training times, while 2D methods may struggle with inter-slice continuity, and fully manual labeling is labor-intensive. Hence, striking a balance between efficiency and accuracy and building lightweight deep-learning models suitable for fracture recognition in volcanic rocks has become a key research direction.

Against this backdrop, we propose a fracture-segmentation workflow transitioning from a 2D random forests models to a 2.5D U-Net + + model, coupled with a semi-automatic “label-as-you-train” strategy, to realize efficient and accurate segmentation of micro-fractures. To ensure the inter-annotator agreement, all labels are made by the author himself. On this basis, we perform skeletonization and pore–throat network modeling to quantify connectivity, and further conduct gas-migration simulations to elucidate controlling mechanisms. The results not only deepen the understanding of the coupling between fractures and migration in volcanic reservoirs, but also provide new theoretical support and technical tools for efficient development and migration prediction in tight reservoirs.

Regional geological setting

Geological background

The Songliao Basin is located in northeastern China, extending from Heilongjiang Province in the north to Liaoning Province in the south. It is NE–SW-trending, 750 km long and 330–370 km wide, with a total area of 2.6×10^5 km^2, and is one of the largest Cretaceous continental petroliferous basins in Asia[11]. Stratigraphically, the basin is dominated by Mesozoic and Cenozoic sedimentary successions, which constitute the principal hosts for hydrocarbon generation, accumulation, and storage in the region[12]. Specifically, the stratigraphic architecture can be divided, from bottom to top, into a Mesozoic succession and a Cenozoic succession (Fig. 1). The Lower Cretaceous comprises, in ascending order, the Huoshiling Formation (K_{1h}), Shahezi Formation (K_{1sh}), Yingcheng Formation (K_{1yc}), Denglouku Formation (K_{1d}), and Quantou Formation (K_{1q}), recording sedimentary infill during the basin’s transition from rifting to post-rift subsidence. The Upper Cretaceous includes the Qingshankou (K_{2qn}), Yaojia (K_{2y}), Nenjiang (K_{2n}), Sifangtai (K_{2s}), and Mingshui (K_{2m}) formations, with depositional facies ranging from deep to shallow lacustrine and deltaic settings, forming multiple source–reservoir–seal assemblages[13]. In the Cenozoic, sedimentation continued with the Paleogene Yian Formation (N_y), and the Neogene Daan (N_d) and Taikang (N_t) formations, followed by the Quaternary Pingyuan Formation (Q)[14]. Overall, the Cretaceous cover of the Songliao Basin contains several vertically stacked petroleum systems with diverse source, reservoir, and seal combinations[15], providing a robust geological foundation for abundant conventional and unconventional hydrocarbon resources.

Geographical location

The Changling fault depression is situated in the central Songliao Basin. Its principal structure trends NE, bounded to the west by the Western Slope Belt and to the east by the Central Depression Belt, and it is among the largest fault-depression units in the basin[16]. The depression is 160 km long (N–S) and 40–60 km wide (E–W), with a total area exceeding 8,000 km^2, making it a key structural unit and hydrocarbon exploration domain in the Songliao Basin.

The Wangfu fault depression lies on the northwestern margin of the Southeastern Uplift Region of the Songliao Basin, structurally occupying the transitional zone between the Changling fault depression and the Southeastern Uplift belt[17]. The area exhibits well-developed tectonics, a complete depositional system, and abundant hydrocarbon resources; it has emerged as a major focus for research as well as exploration and development activities with significant scientific and economic potential.

The Dehui fault depression is located in the southern part of the basin within the Southeastern Uplift. It is bounded by the Yitong Graben to the east, the Lishu fault depression to the south, the Denglouku anticline belt to the west, and the Wangfu fault depression to the north. The depression is elongate and NE–SW-trending, with strata ranging from the Huoshiling to the Nenjiang formations. Multiple reservoir–seal assemblages are developed, and hydrocarbon enrichment is governed by coupled fault–lithology controls, making it one of the important producing areas[18].

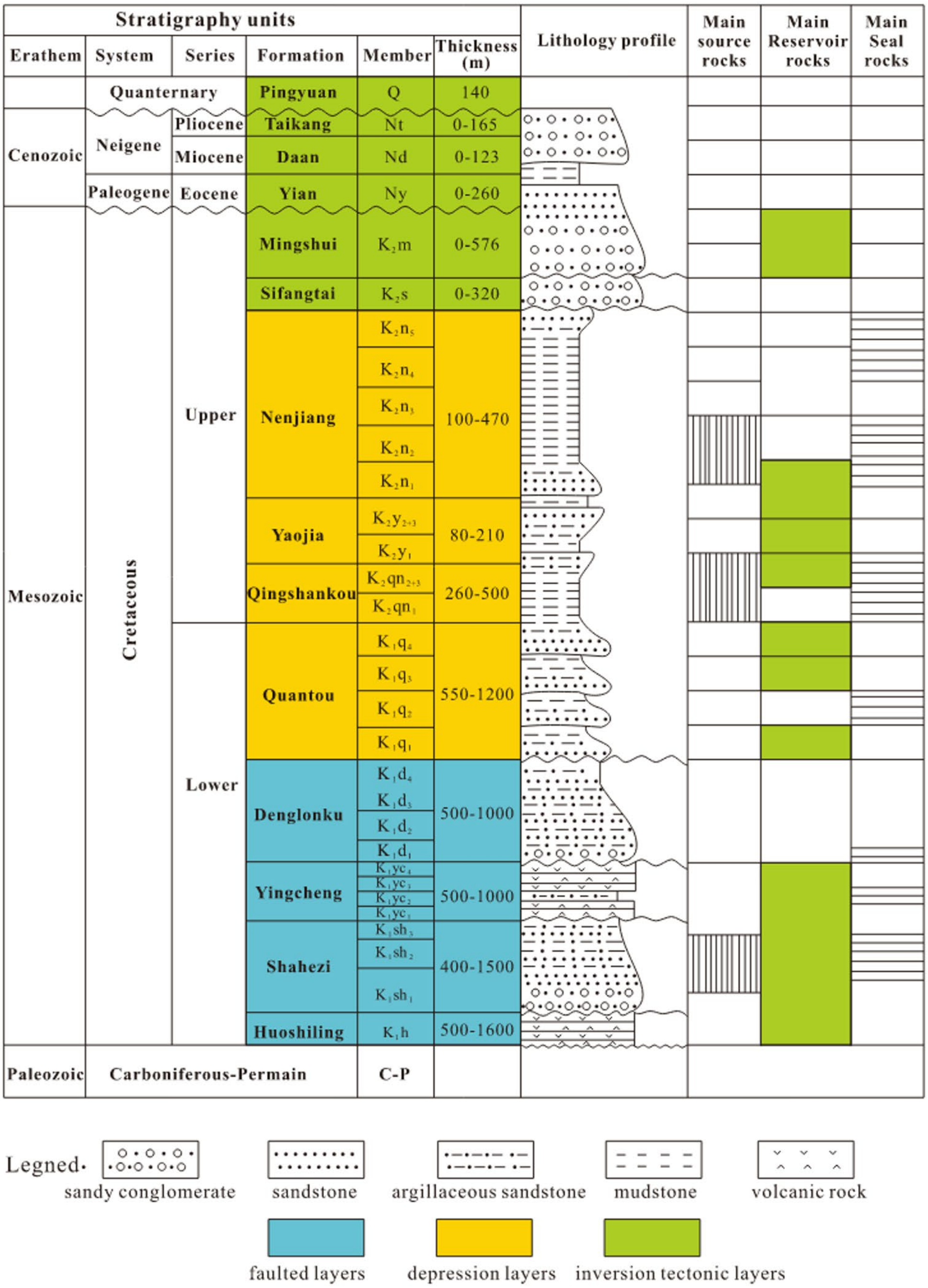

Fig. 1. Stratigraphic framework of the Songliao Basin, highlighting the principal source rocks and reservoir intervals. (modified from Gao et al.[6]. This image was edited in CorelDRAW (Version:24 5.0.731.URL: https://www.coreldraw.com/cn).

In this study, four representative volcanic-reservoir core samples—CS1, W21, CS105, and DS9—were selected from the Changling, Wangfu, and Dehui fault depressions of the Songliao Basin (Fig. 2).

Samples and methods

Rock samples and μCT imaging

Rock samples

We chose 4 volcanic core samples of the Yingcheng Formation in the southern Songliao Basin from the Jilin Oilfield E&D Research Institute, PetroChina, among which 2 of the samples came from the Changling Fault Depression (well of CS1, CS105), 1 sample came from Dehui Fault Depression (well of DS9) and 1 sample comes from Wangfu Fault Depression (well of W21), all these samples were tested for the reservoir physical

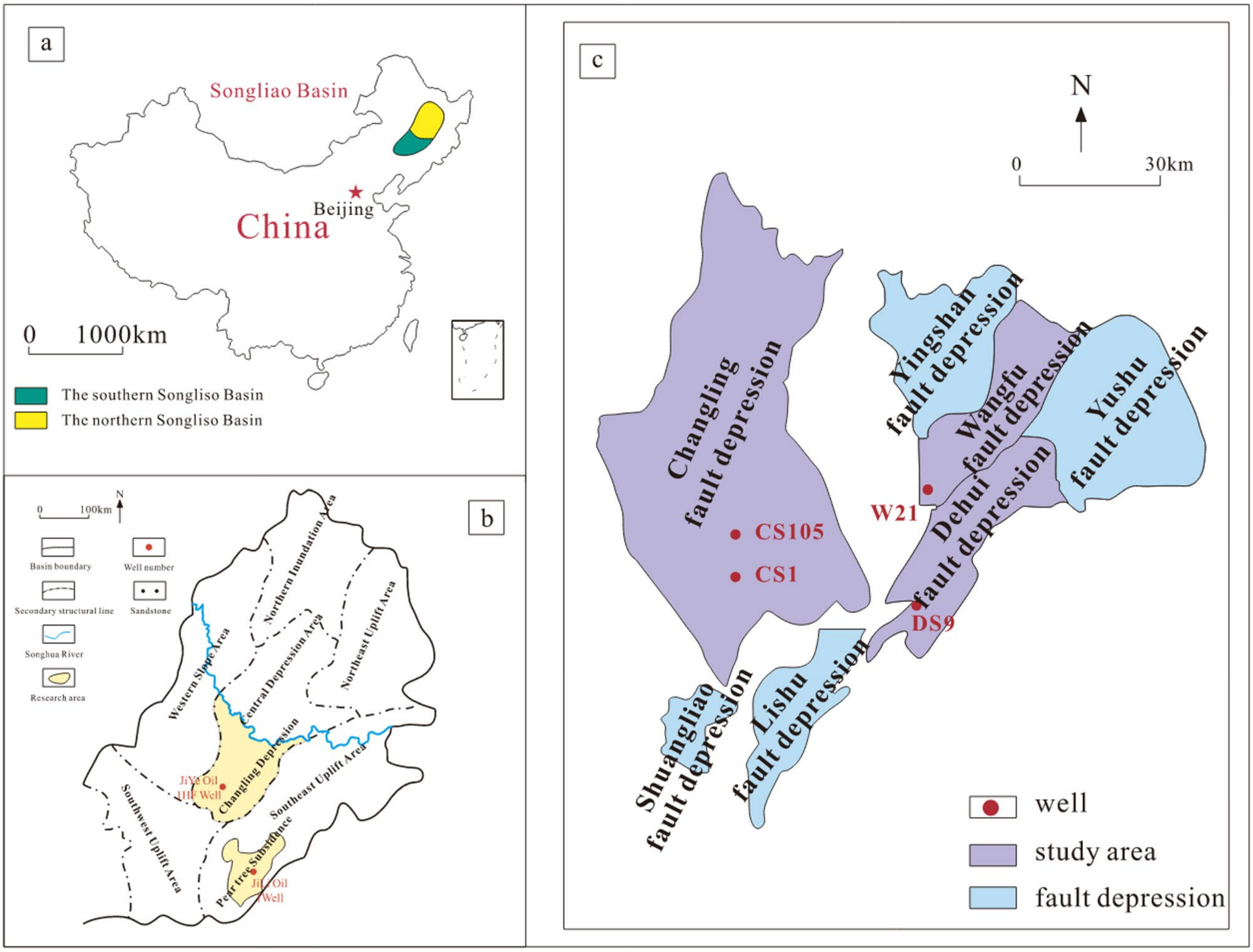

Fig. 2. Schematic map of fault depressions: (**a**) location of the Songliao Basin in China; (**b**) principal structural units of the Songliao Basin; (**c**) locations of the Changling, Wangfu, and Dehui fault depressions. (modified from Wang et al.[19]. This image was edited in CorelDRAW (Version: 24 5.0.731.URL: https://www.coreldraw.com/cn.)

property determination. In order to further study the petrophysical properties and microscopic fracture system of volcanic reservoirs with the abnormal negative correlation between porosity, permeability and natural gas diffusion coefficient, the volcanic samples CS1(3,574.15 m) and W21(1,399 m) are chosen as one comparison, CS105 (3,926.57 m) and DS9 (2010.60 m) are chosen as another comparison group for further CT scanning determination.

CS1 is a rhyolitic crystal-lithic tuff (Fig. 3a) composed of crystal fragments, lithic fragments, and volcanic ash, with crystal and lithic fragments totaling 80%. The dominant minerals are quartz and alkali feldspar, and local kaolinitization and sericitization are observed.

W21 is a trachyandesitic crystal-lithic tuff (Fig. 3b). Clastic components account for 30%, dominated by plagioclase and quartz; dissolution pores are developed, together with sericitization.

CS105 is a volcanic tuff (Fig. 3c) with volcanic ash contents up to 95%, showing a dense matrix; local carbonate alteration is present.

DS9 is a porphyritic andesite (Fig. 3d). Phenocrysts are mainly feldspar (15%), and the matrix is also feldspar-rich, with intense alteration.

Collectively, these sample types span lithologic assemblages representing different porosity and permeability conditions in volcanic reservoirs (Table 1), providing a basis for analyzing fracture architectures under varying diagenetic settings.

μCT imaging

μCT imaging exploits differences in X-ray attenuation arising from mineral-density contrasts to achieve non-destructive three-dimensional reconstruction of internal rock structures[20]. The scanning system comprises an X-ray source, a detector, and a rotary stage (Fig. 4a), enabling precise capture of intracore microstructures. In this study, scans were acquired using a phoenix vltomel xm industrial CT system at a spatial resolution of 12 μm with cylindrical samples of 2.5 cm diameter. The tube-voltage range was 160–240 kV, and the scan field was 450

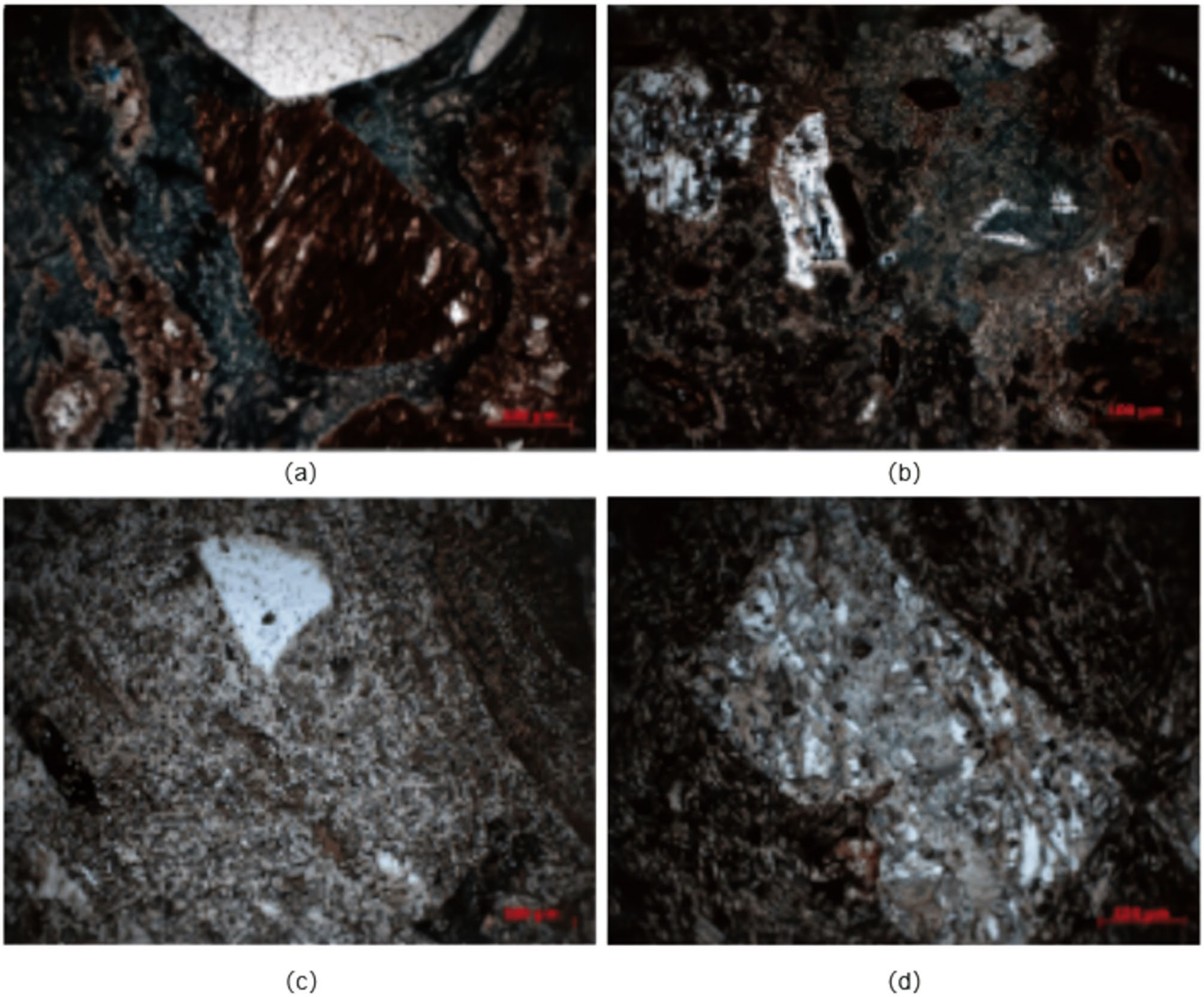

Fig. 3. Photomicrographs of samples: (**a**) rhyolitic crystal–lithic tuff from well CS1; (**b**) dacitic crystal–lithic tuff from well W21; (**c**) volcanic tuff from well CS105; (**d**) porphyritic andesite from well DS9.

Well	Depth (m)	Lithology	Permeability (mD)	Porosity (%)	CH_4 Diffusion coefficient (cm^2/s)
CS1	3574.15	Rhyolitic crystal tuff	0.11	12.6	7.66×10^{-6}
CS105	3926.57	Volcanic tuff	0.0077	2.3	7.78×10^{-6}
W21	1399.00	Trachyandesite Crystal tuff	0.02	5.4	1.51×10^{-6}
DS9	2010.60	Porphyritic andesite	0.00017	3.3	4.81×10^{-7}

Table 1. Measured petrophysical properties of volcanic reservoir samples (CS1, W21, CS105, DS9).

× 350 mm. Projection data were reconstructed and sliced in VGStudio MAX, yielding high-resolution 2D CT images (Fig. 4b) with technical support from Sanying Testing (Tianjin, China).

Ensemble-learning-based 2D fracture segmentation

Fractures and matrix in volcanic-rock μCT images exhibit low contrast and complex morphologies; consequently, image preprocessing and feature optimization are required prior to segmentation. The end-to-end training workflow comprises three stages: image preprocessing, region-of-interest (ROI) extraction, and Random-Forest–based segmentation model training (Fig. 5).

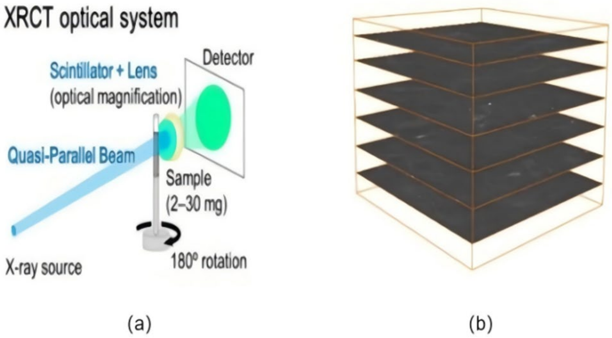

(a) (b)

Fig. 4. Schematic of the X-ray computed tomography (XRCT) system: (**a**) basic layout of the XRCT setup with an imaging volume of 244 mm × 195 mm and a detector array of 1920 × 1536 pixels. (modified from[21]. This image was edited in Axure PR9 (Version:9. URL: http://www.axure.com.); (**b**) representative XRCT slice image.

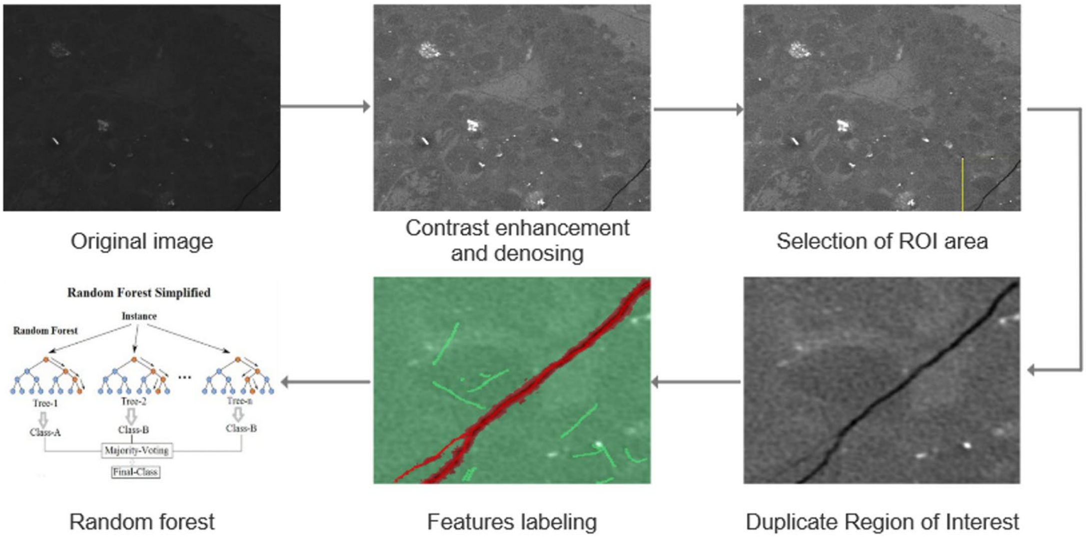

Fig. 5. 2D fracture-preprocessing and segmentation workflow for volcanic-rock samples (CS1 example). In the CT slice, white denotes mineral grains, gray represents the volcanic-reservoir matrix, and black corresponds to pores and fractures.

Preprocessing of Raw μCT slices

Raw μCT slices exhibit low grayscale contrast (Fig. 6a), which hampers fracture delineation[22]. We first applied linear contrast stretching to enhance separation between mineral phases and pore–fracture voids (Fig. 6b), and then used a 3 × 3 median filter to suppress noise while preserving edge detail (Fig. 6c).

To improve computational efficiency, representative regions of interest (ROI) were selected for each sample (Fig. 7). Feature labeling and model training were then confined to these ROIs, thereby reducing data redundancy[23,24].

Random forest architecture and training

In this study, we use the Random Forest algorithm to segment fractures. By ensembling multiple decision trees and determining the class by majority voting, the algorithm effectively reduces overfitting and improves segmentation robustness[25]. Its mathematical formulation is as follows:

$$\widehat{y}_i = \mathrm{mode}\left\{h_1(f(x_i)), h_2(f(x_i)), \ldots, h_n(f(x_i))\right\} \tag{1}$$

where $\widehat{y}_i$ denotes the pixel's segmentation class, $f(x_i)$ is its feature vector, mode is the mode operator, and h_j denotes the j-th decision tree (base learner). The random forest feeds the same fracture sample into each tree and tallies the class votes across base learners to obtain the final prediction (Fig. 8).

During training, we propose a semi-automatic “label-as-you-train” strategy:

(1) From every 200 slices, one slice was selected for training, and fractures and non-fracture regions were manually labeled (Fig. 9a,c).

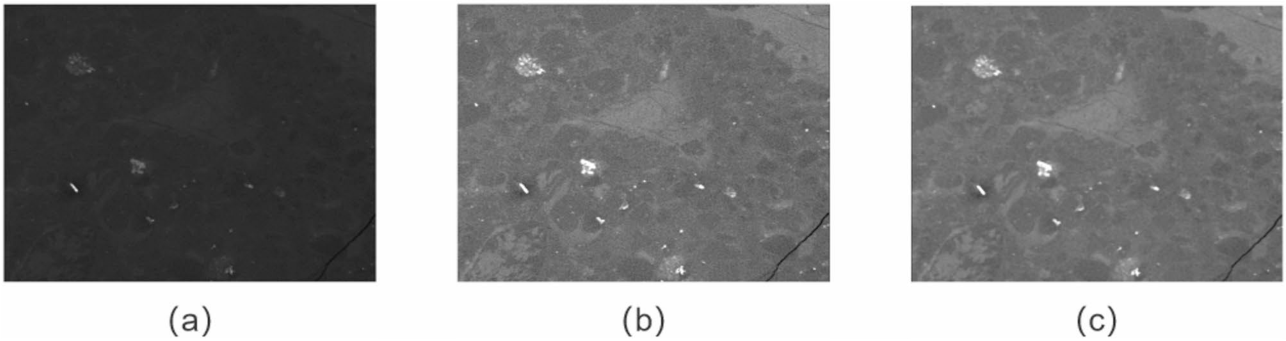

Fig. 6. Preprocessing workflow for 2D volcanic-rock samples (CS1 example): (**a**) raw slice; (**b**) after linear contrast stretching; (**c**) after 3 × 3 median filtering.

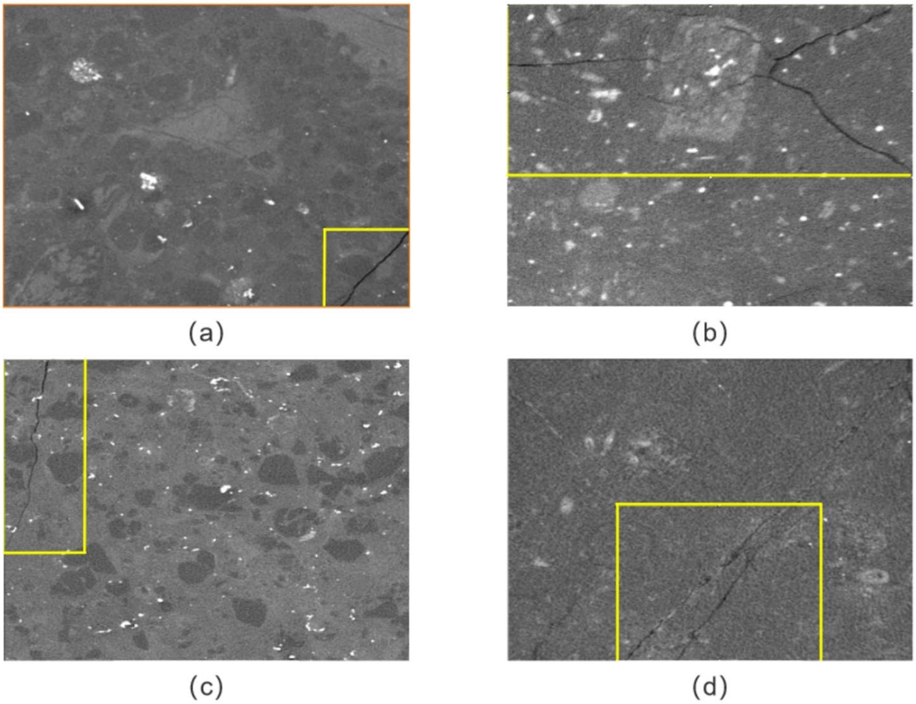

Fig. 7. Locations of selected regions of interest (ROI) in 2D volcanic-rock samples: (**a**–**d**) correspond to CS1, W21, CS105, and DS9, respectively.

(2) An initial Random Forest model was trained on the annotated samples (Fig. 9b,d).
(3) The model was applied to new slices; At this time, we would also choose one slice from every 200 slices to manually correct misclassified regions and retrain the new model.
(4) The iteration was repeated, and the final trained model was applied to all slices.

This approach substantially reduces manual annotation costs and rapidly yields reasonably accurate fracture segmentations (Fig. 10). However, because 2D models struggle to capture axial continuity, some fine fractures remain misidentified. Thus, further optimization with deep learning models is required[26].

2.5D deep-learning fracture segmentation

To optimize segmentation, the "coarse-to-fine" hybrid strategy is implemented: After Random Forest initially mitigates class imbalance by filtering background noise and partial pores, we provide a robust prior for 2.5D U-Net++ refinement. The 2.5D architecture was prioritized over full 3D models to achieve a superior trade-off between computational efficiency and accuracy. By leveraging inter-slice context, 2.5D kernels effectively capture spatial dependencies while significantly reducing memory overhead and the demand for exhaustive 3D manual annotations—a critical bottleneck in volcanic fracture characterization. This integration ensures high-fidelity topological reconstruction while maintaining model generalizability under limited annotated samples.

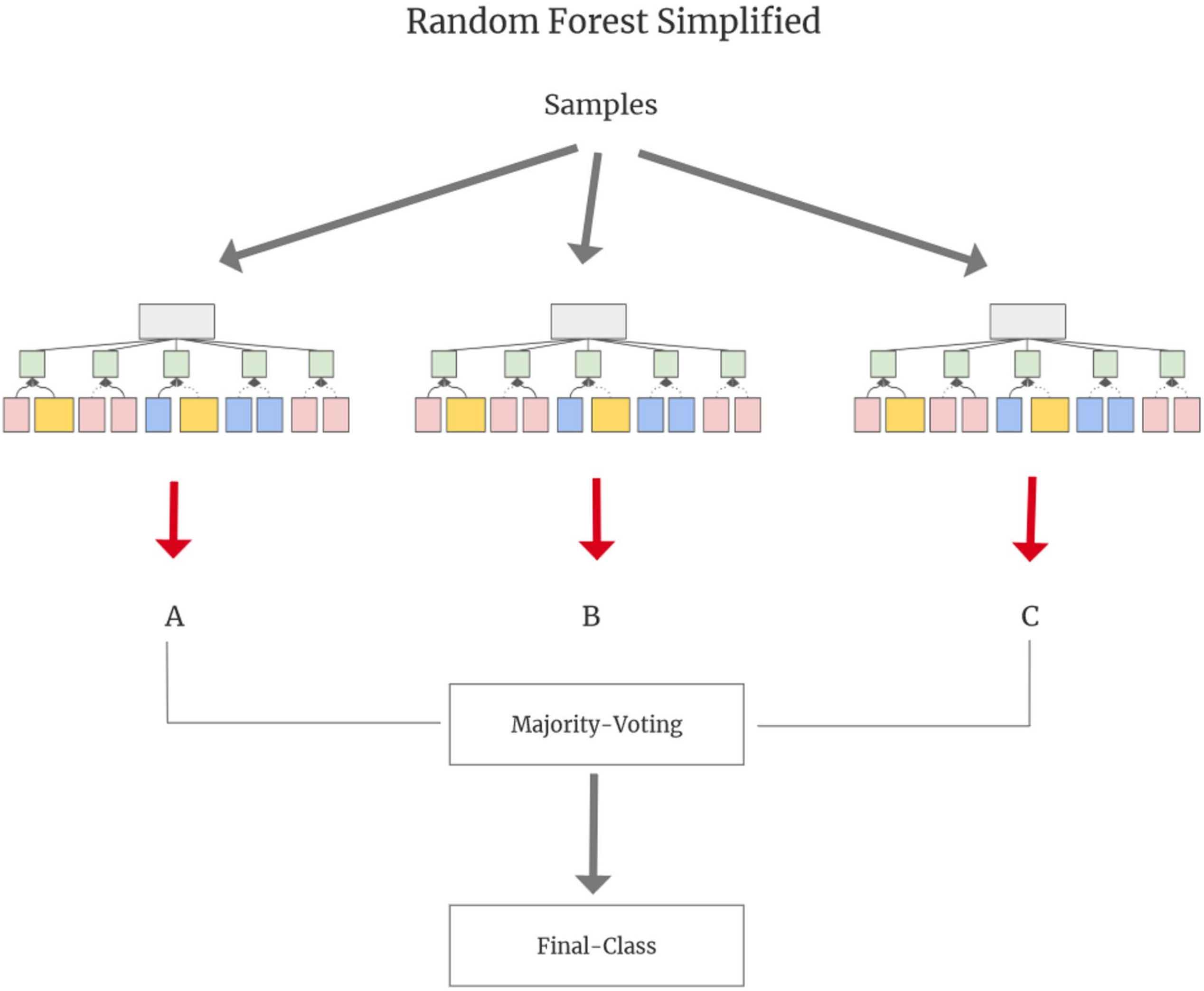

Fig. 8. Architecture of the Random Forest model: feature vectors from μCT ROIs are input to an ensemble of decision trees; each tree outputs a class, and majority voting yields the final fracture/non-fracture segmentation.

However, given that there still remain high computational demands of 2.5D deep-learning models, samples must be preprocessed prior to segmentation[27]. The end-to-end training workflow comprises three stages: construction of the 3D grayscale volume, region-of-interest extraction, and training of a 2.5D U-Net + + segmentation model (Fig. 11).

Construction of the 3D grayscale volume

Construction of a 3D grayscale volume is achieved by serially stacking grayscale images, thereby reconstructing a three-dimensional dataset that preserves spatial distribution information[28]. In this study, we stacked all 2D slices segmented by the Random Forest model (Fig. 12a) to generate the 3D grayscale volume (Fig. 12b).

2.5D U-Net++: architecture and training

The U-Net deep learning model (Fig. 13) is a convolutional neural network (CNN)–based segmentation architecture designed specifically for pixel-level image segmentation[29]. It adopts an encoder–decoder structure and employs skip connections to fuse multi-level semantic and spatial information, thereby accomplishing the segmentation task[30].

Building on this, U-Net++ (Fig. 14) introduces densely nested skip connections and nested submodules, substantially enhancing feature representation and boundary delineation[31].

The 2.5D U-Net + + model combines the strengths of 2D and 3D representations. By using multi-channel inputs from adjacent slices, it captures through-plane continuity while keeping computational load relatively low, thereby enabling high-accuracy segmentation[32,33].

During training, we continue to employ a semi-automatic “label-as-you-train” strategy:

(1) The training dataset comprises axial regions formed by stacking nine adjacent slices. Fractures, pores, and air are labeled in purple, green, and orange, respectively (Fig. 15).

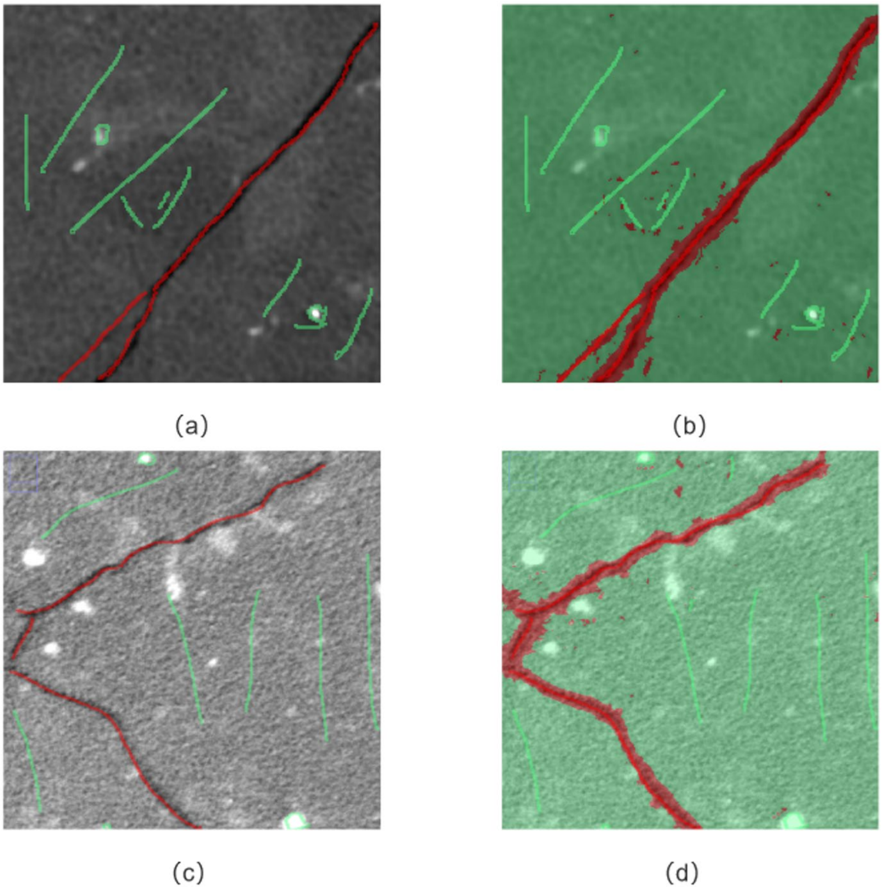

Fig. 9. µm-scale 2D volcanic-rock sample annotation and training workflow: (**a**) and (**c**) show manual labeling for samples CS1 and W21, where red marks fractures and green marks pores and other matrix; (**b**) and (**d**) show the pore–fracture segmentation results after training the ensemble-learning model, with red indicating the segmented fractures.

(2) The model adopts a 2.5D input configuration, a five-level encoder–decoder depth, a batch size of 8, and the Adadelta optimizer to train the initial U-Net + + model.

(3) Apply the model to the remaining axial regions; At this time, we also choose an axial region formed by stacking nine adjacent slices to manually correct misclassified areas, retrain, and iterate until stable convergence is achieved.

The 2.5D U-Net + + model effectively distinguishes fracture–pore boundaries, producing a more continuous and realistic fracture network (Fig. 16). By combining the Random Forest and U-Net + + models, we ultimately achieve a balance between computational efficiency and segmentation accuracy.

Quantitative 3D fracture analysis and gas-flow simulation

Principles and processes of 3D modeling

(1) Connectivity analysis: We import the final-segmented micro-fracture model (Fig. 17a) into Avizo (2020.1, Thermo Fisher Scientific, Waltham, MA, USA) to get the further study about it, and the Remove Small Islands module was applied to eliminate noise and artifacts and to generate a 3D binary fracture model (Fig. 17b). To characterize fracture connectivity, a 26-neighborhood scheme was adopted (Fig. 17c), and the Axis Connectivity module was used to identify and quantify connected fracture structures.

(2) Pore–throat network modeling: Using the maximal inscribed-sphere algorithm (Fig. 18a), the complex fracture system is abstracted into a pore–throat network (Fig. 18b)[34]. The Generate Pore Network Model module in Avizo was then used to compute pore and throat sizes and their connectivity, enabling quantitative characterization of the fracture system's storage and transport capacity.

(3) Fracture-network skeletonization: An iterative thinning algorithm was employed to extract fracture skeletons, simplifying morphology while preserving topological structure[36]. The Auto Skeleton and Spatial Graph View modules in Avizo were used to visualize internal dissolution features and connection pathways.

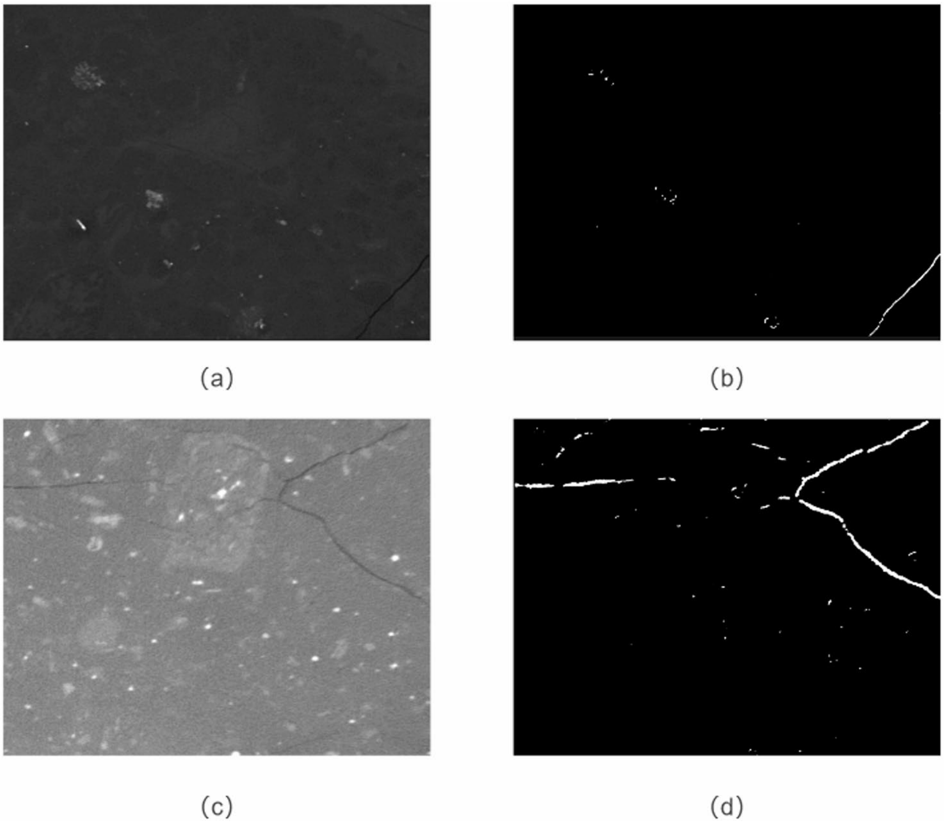

Fig. 10. µm-scale comparison of 2D fracture-segmentation results for volcanic-rock samples: (**a**) and (**b**) show CS1 raw slice and corresponding fracture-segmentation map; (**c**) and (**d**) show W21 raw slice and corresponding fracture-segmentation map.

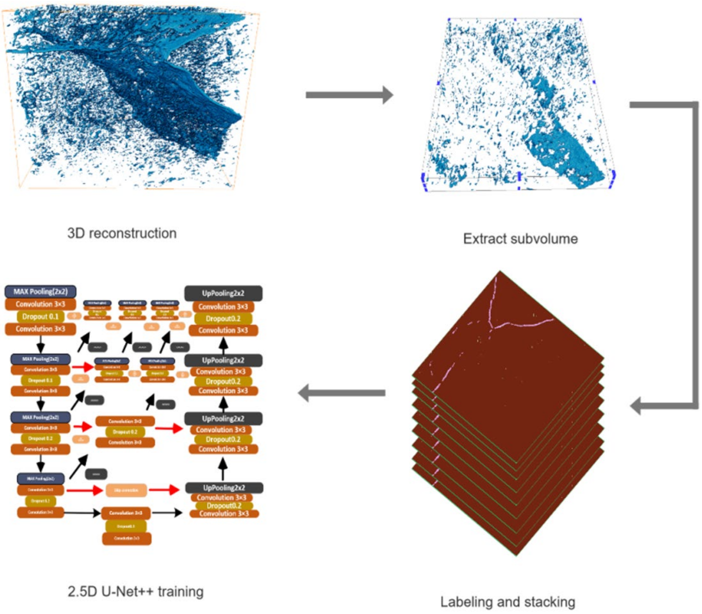

Fig. 11. 2.5D fracture-segmentation workflow for volcanic rocks (W21 example). In the CT slice, green denotes pores, purple denotes fractures, and red denotes air. The 3D digital rock core is reconstructed by stacking a series of 2D slices.

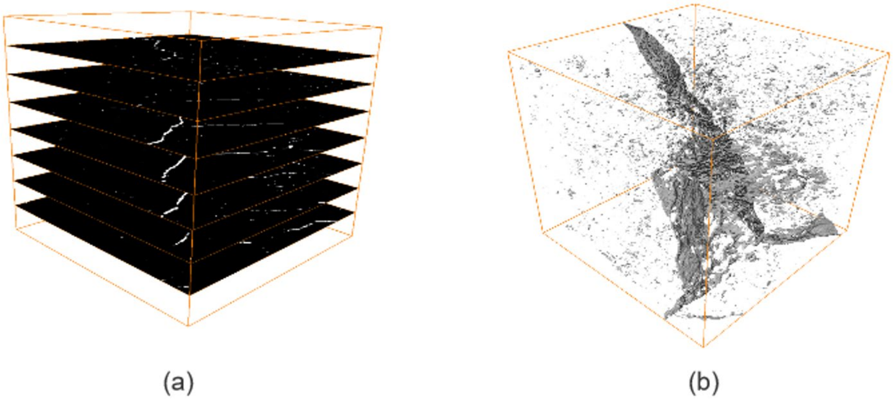

Fig. 12. Schematic of 3D grayscale volume construction: (**a**) stacking workflow of 2D slices; (**b**) reconstructed 3D grayscale volume.

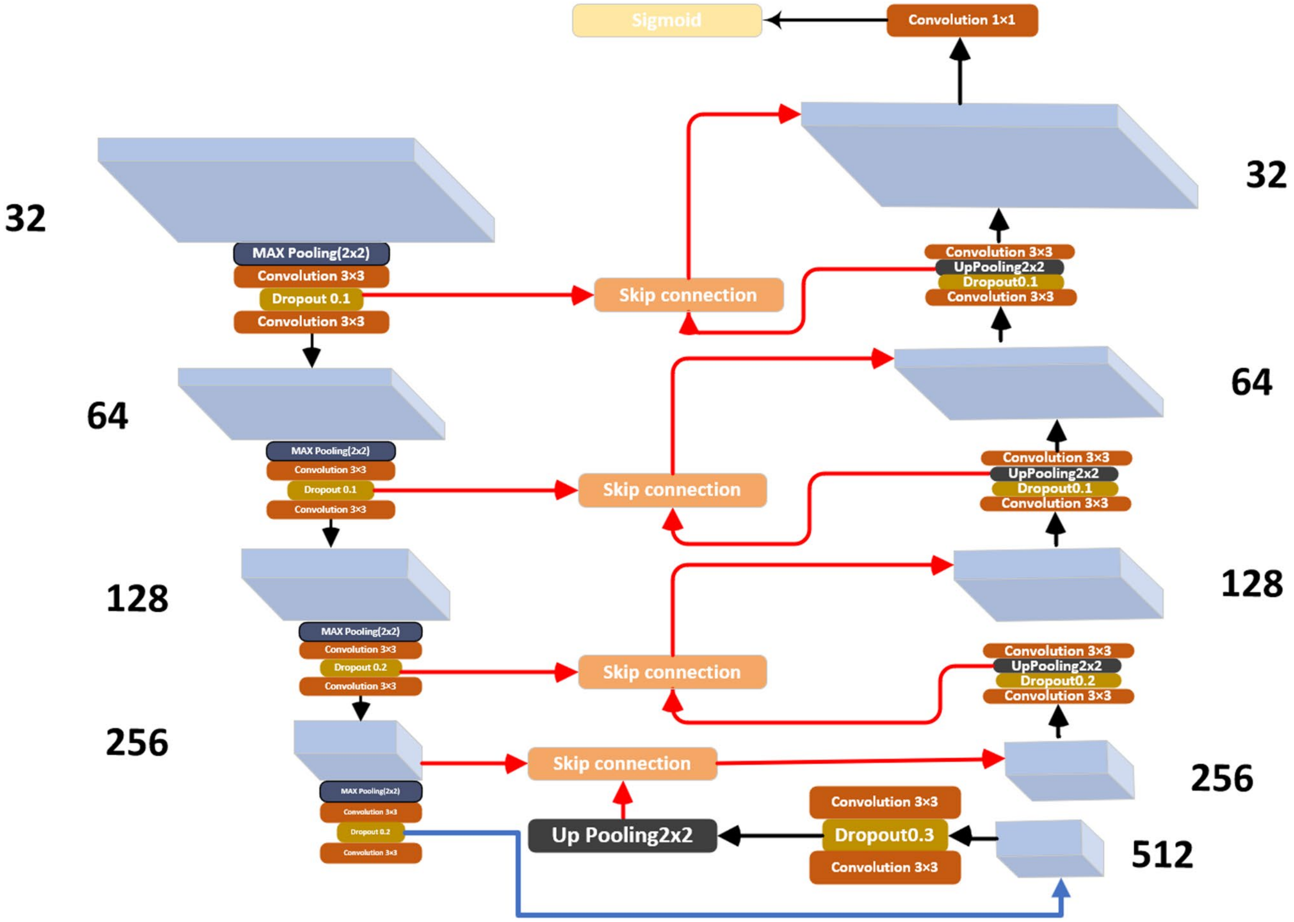

Fig. 13. The Architecture of U-Net.

Natural gas seepage simulation

Based on Darcy's law (2), gas seepage was numerically simulated in Avizo using the "Absolute Permeability Experiment Simulation" and "Illuminated Streamlines" modules. To be noted that firstly, at the micrometer scale, the Reynolds Number (Re) of fluid flow is extremely low, ensuring that it remains in the linear laminar regime where Darcy's law applies and second, although gasses exhibit compressibility and slip effects (Klinkenberg

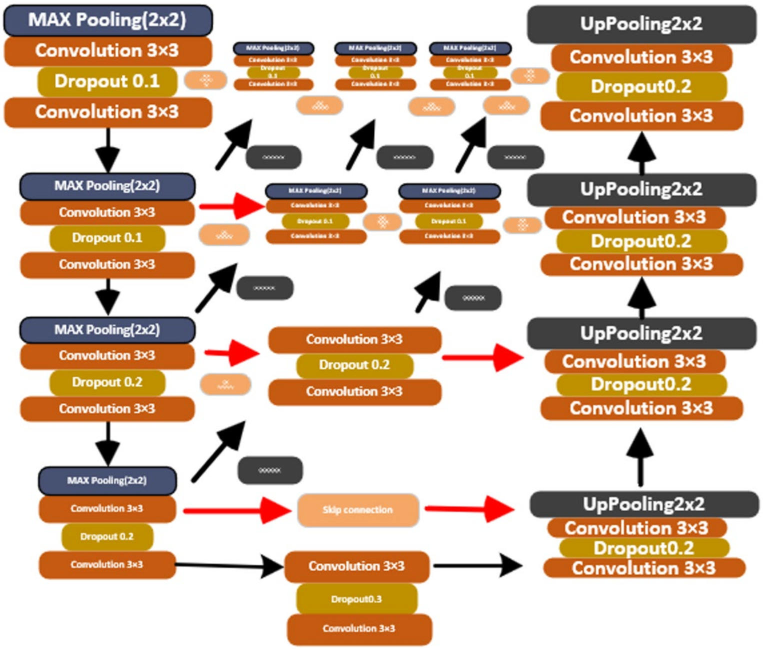

Fig. 14. The architecture of U-Net ++.

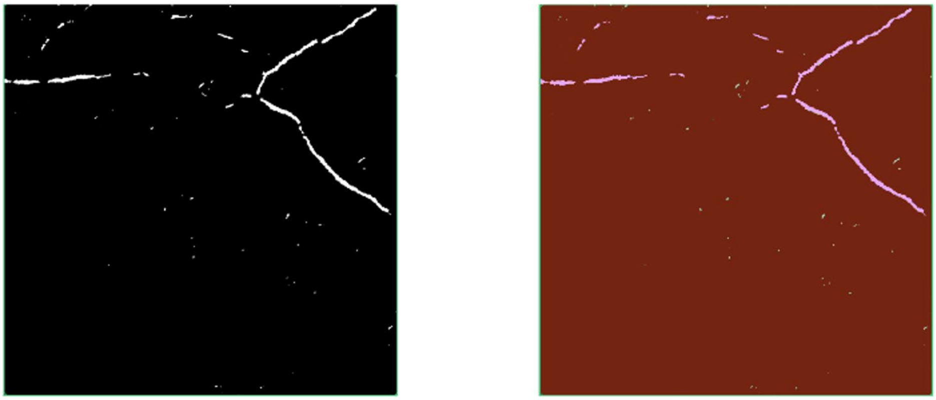

(a)

(b)

Fig. 15. Schematic of the deep-learning dataset annotation workflow. Red denotes air, green denotes pores, and purple denotes fractures.

effect) at low pressures or in extremely small pores, these effects are relatively limited for the micrometer-scale fractures identified in this study[37].

$$Q = -\frac{kA}{\mu}\frac{\Delta P}{L} \tag{2}$$

where Q denotes the volumetric flow rate (μm³/s), k the rock permeability (mD), A the cross-sectional area (μm^2), μ the fluid viscosity (Pa·s), ΔP the inlet–outlet pressure difference (MPa), and L the flow-path length (μm). We set the inlet pressure to 3.5 MPa, the outlet pressure to 0.1 MPa, and the fluid viscosity to 1.087×10^{-5} Pa s, then computed the permeability and velocity distributions for each sample to characterize the fluid flow field at the micrometer scale.

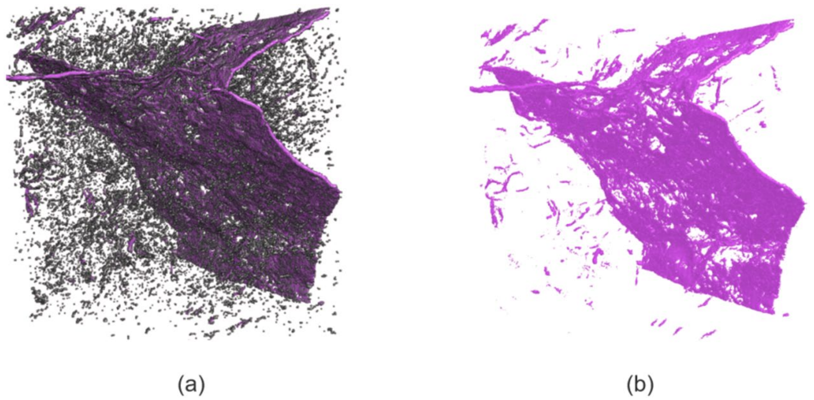

(a) (b)

Fig. 16. µm-scale comparison of 3D fracture-segmentation results for the W21 sample: (**a**) fracture network segmented by the ensemble-learning model; (**b**) fracture network segmented by the deep-learning model (2.5D U-Net++).

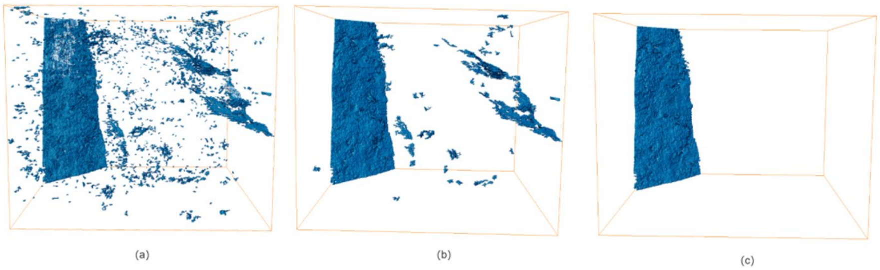

(a) (b) (c)

Fig. 17. 3D fracture-distribution model: (**a**) initial 3D digital rock-core reconstruction after threshold segmentation; (**b**) denoised 3D digital rock-core model; (**c**) 3D model of connected fractures.

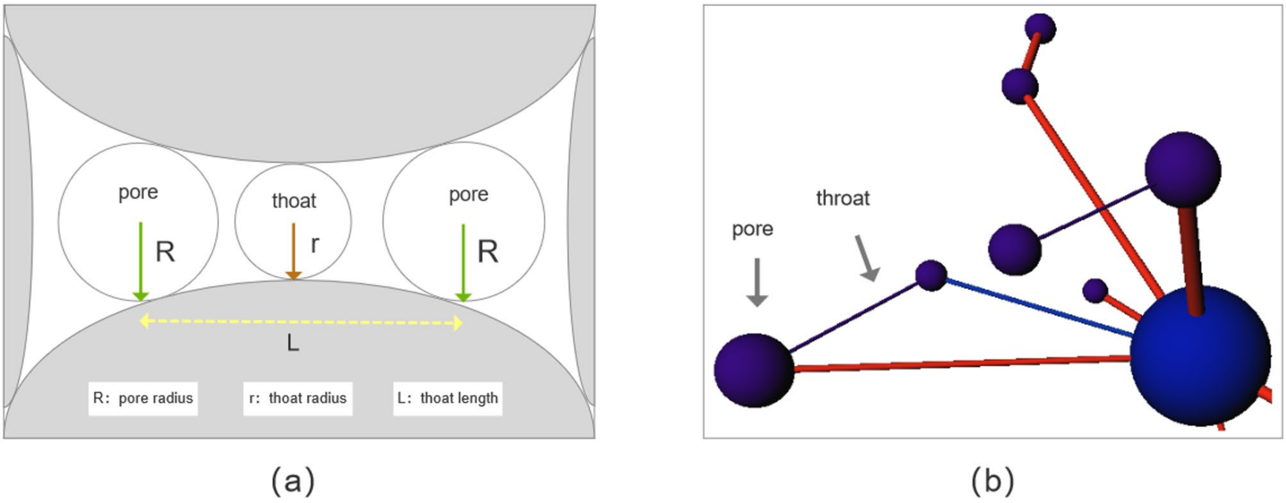

Fig. 18. Maximal inscribed-sphere construction and pore–throat structure: (**a**) schematic of the maximal inscribed-sphere construction. (modified from Zhao et al.[35].This image was edited in Axure PR9 (Version:9. URL: http://www.axure.com.) ; (**b**) schematic of the pore–throat structure.

Results

Model performance and comparison

Using sample W21, we illustrate the training outcome of the 2.5D U-Net++model. Figure 19 shows the evolution of the loss and Dice coefficient on the training and validation sets. The loss decreases sharply during the first two epochs and then tapers off. By epoch 10, the Dice coefficient reaches 0.902. Since the Dice

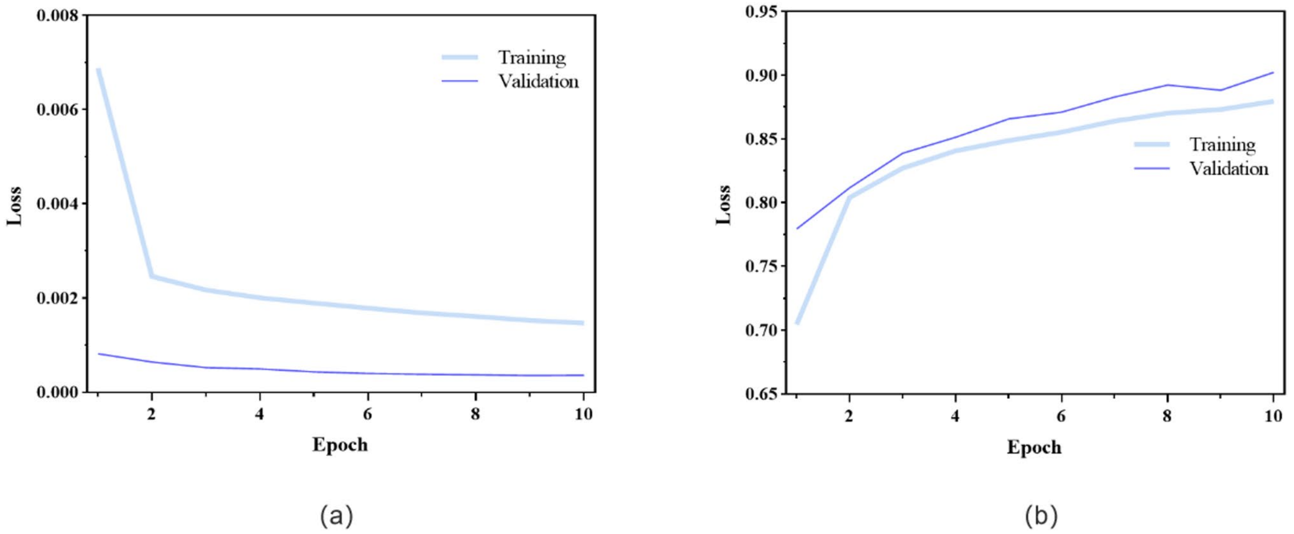

Fig. 19. Training and validation curves for the 2.5D U-Net + + model (W21): loss and Dice versus epoch.

Epoch	U-Net	U-Net++	Trans-Unet	Link-Net	I-Net
5	0.37	0.39	0.35	0.27	0.31
10	0.43	0.51	0.67	0.32	0.37
5*	0.78	0.85	0.57	0.28	0.33
10*	0.83	0.90	0.79	0.33	0.47

Table 2. Model training results. Note: * indicates pre-segmentation by the Random Forest model.

coefficient comprehensively balances pixel-level precision and recall, it serves as a robust metric for evaluating the segmentation quality of complex fracture networks. It is worth noting that, in binary segmentation tasks, Dice is significantly positively correlated with IoU as follows.

$$IoU = \frac{Dice}{(2 - Dice)} \tag{3}$$

Calculations indicate that the equivalent IoU of this model is approximately 0.821. Considering time-to-result constraints, we concluded the model training at this point.

Table 2 reports the final training outcomes of five models on sample W21, including U-Net++. Across all models, applying the Random Forest pre-segmentation consistently yielded higher accuracy. Among the deep-learning models, the 2.5D U-Net + + achieved the best performance with a Dice coefficient of 0.90, followed by the 2D U-Net at 0.83. In contrast, Link-Net was also employed as a baseline to evaluate the performance of lightweight architectures in fracture segmentation. Its poor performance, with a Dice coefficient of 0.33, underscores the limitations of simple additive skip connections in preserving the delicate topology of micro-fractures. Compared to the nested structure of U-Net++, Link-Net struggles to fuse multi-scale semantic features effectively, especially under low-contrast conditions typical of volcanic rocks.

Figure 20 compares the training times of the models. As shown, samples pre-segmented by the Random Forest model exhibit faster training across all models. The 2.5D U-Net has a training time between U-Net and I-Net. Link-Net is the fastest at 3 min, whereas I-Net is the slowest at 189 min.

Three-dimensional fracture morphology and connectivity

By comparing the 3D connected-pore and 3D connected-fracture distribution models (Fig. 21), the statistical analysis (Table 3) shows that, at the micrometer scale, the total pore volume of sample CS1 is 165.65 μm^3, with a total surface area of 11,601.61 μm^2. Among these, the connected pore volume is 112.02 μm^3 and the connected fracture volume is 7.37 μm^3, accounting for 67.6% and 4.44% of the total pore volume, respectively. For W21, the total pore volume is 76.56 μm^3, with a total surface area of 9,903.83 μm^3. The connected pore volume is 52.43 μm^3 and the connected fracture volume is 7.38 μm^3, accounting for 68.5% and 9.91% of the total pore volume, respectively. In summary, sample CS1 not only possesses a larger pore storage space, but also contains a well-connected fracture network, allowing natural gas to be distributed more broadly within the reservoir and to migrate rapidly along well-developed fractures. In contrast, although W21 exhibits a larger fracture surface area, its fractures are less developed and structurally discrete; the slender, tortuous network is unlikely to form efficient migration pathways for natural gas, thereby reducing the effective permeability of the reservoir.

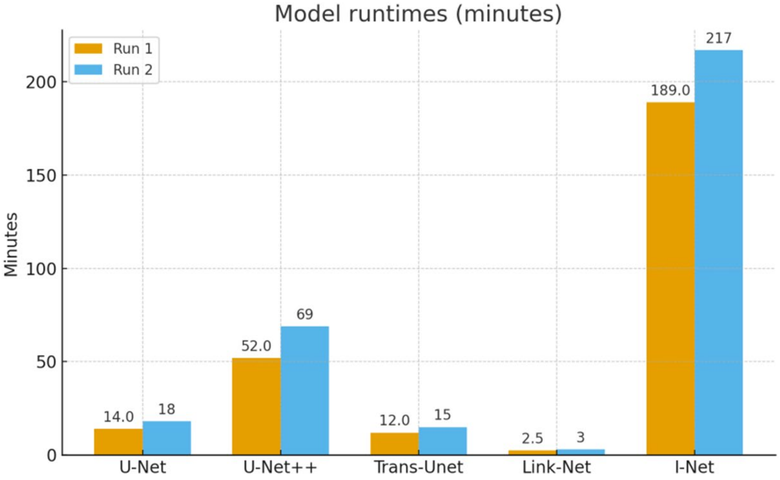

Fig. 20. Model training time: Run1 denotes training time with Random Forest pre-segmentation; Run2 denotes training time for direct deep learning. The number of training epochs is 10.

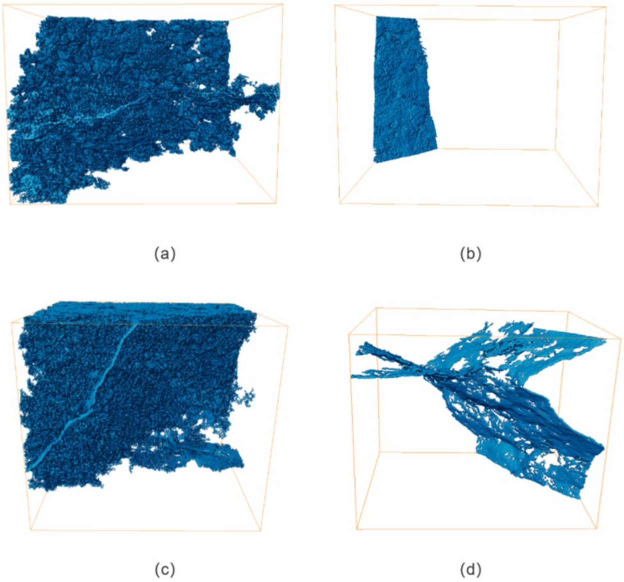
(a) (b) (c) (d)

Fig. 21. 3D distributions of connected pores and fractures: (**a**) and (**c**) show the 3D distributions of connected pores for CS1 and W21, respectively; (**b**) and (**d**) show the 3D distributions of connected fractures for CS105 and DS9, respectively.

Parameter	CS1 sample	CS1 connected fractures	W21 sample	W21 connected Fractures
Total volume (μm^3)	165.66	7.37	76.56	7.37
Total surface area (μm^2)	11601.61	149.10	9903.83	338.41
Connected pore volume (μm^3)	112.02	–	52.44	–
Connected pore area (μm^2)	6541	–	6051.49	–

Table 3. Pore-fracture parameters for CS1 and W21. Note: CS1 denotes a rhyolitic crystal–lithic tuff, and W21 denotes a dacitic crystal–lithic tuff.

Model comparison (Fig. 22) and experimental results (Table 4) show that, at the micrometer scale, the total pore volume of sample CS105 is 279.39 μm^3, while the total volume of its connected fractures is 24.87 μm^2, with a connected-fracture ratio of 8.9%, which is much higher than the 10.48 μm^3 of fractures in DS9. A comprehensive analysis indicates that the larger connected-pore volume and connected-fracture volume within CS105 provide

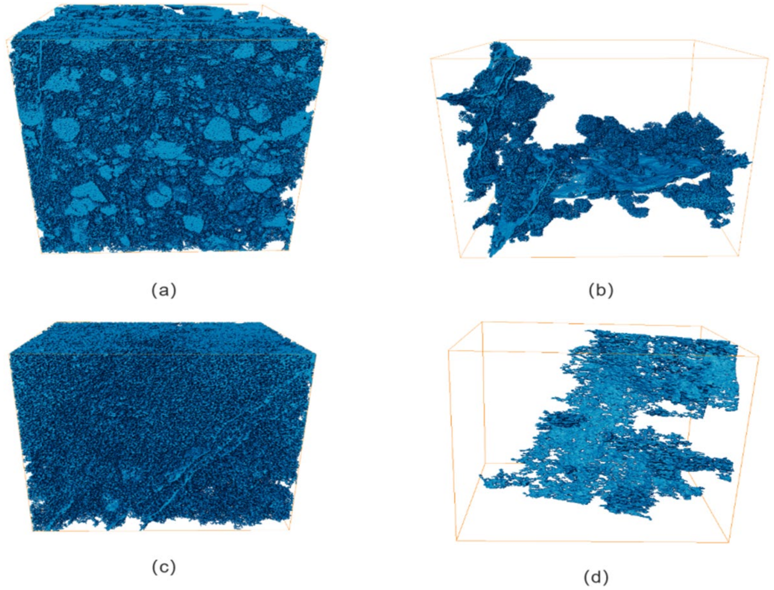

Fig. 22. 3D distributions of connected pores and fractures: (**a**) and (**c**) show the 3D distributions of connected pores for CS105 and DS9, respectively; (**b**) and (**d**) show the 3D distributions of connected fractures for CS105 and DS9, respectively.

Parameter	CS105 Sample	CS105 Connected Fractures	DS9 Sample	DS9 Connected Fractures
Total volume (μm^3)	279.39	24.87	165.44	10.48
Total surface area (μm^2)	20013.72	2495.84	15012.94	422.87
Connected pore volume (μm^3)	241.97	–	143.27	–
Connected pore area (μm^2)	15199.08	–	11592.59	–

Table 4. Pore–fracture parameters for CS105 and DS9. Note: CS105 denotes a volcanic tuff, and DS9 denotes a porphyritic andesite.

a broader three-dimensional space for natural gas storage and transport, whereas the fracture structure of DS9 is fragmented, making it difficult to form efficient percolation pathways for natural gas.

Pore–throat network characteristics

To further analyze the connection efficiency and structural characteristics of fracture bodies within the percolation network of volcanic reservoirs, a 3D pore–throat network model was used to characterize the integrity and transport capacity of the fracture structures in the two sample sets (Fig. 23)[38]. Red spheres represent pores, and yellow tubes represent throats.

At the micrometer scale, fractures in CS1 exhibit larger pore sizes and a relatively dense distribution of throats, indicating good connectivity, whereas fractures in W21 have slender, dispersed throats, with instances of pore–throat disconnection. In the other sample set, fractures in CS105 likewise display wide pores and throats with strong throat continuity and a tendency toward overall connectivity. By contrast, DS9 has a greater number of pores and throats, but the throats are slender and the pore sizes are very small, which is unfavorable for efficient natural-gas transport in this region.

By performing quantitative calculations on the resulting pore–throat network model, we obtained physical parameters including total pore volume, throat surface area, coordination number, and others (Table 5).

Quantitative calculations show that the average pore radius of CS1 fractures is 0.22 μm, and the average throat radius is 0.13 μm, which are 1.29 and 2.03 times those of W21, respectively. Although W21 fractures have a larger total pore surface area and throat length, the internal throats are slender and dispersed, making it difficult to develop efficient longitudinal pathways for natural gas migration. The results indicate that, compared with W21, CS1 fractures have a higher average coordination number and larger pore and throat widths, exhibiting stronger spatial interconnectivity and favoring natural-gas flow and storage. In the other sample set, the total volume of CS105 fractures is 24.87 μm, which is 2.37 times that of DS9; the average pore radius is 0.44 μm, and the average throat radius is 0.11 μm, which are 3.39 and 2.12 times those of DS9, respectively. The experimental results show that, relative to DS9, CS105 fractures possess wider pore–throat radii, greatly reducing resistance during natural-gas migration and enabling rapid, large-volume transport in this region.

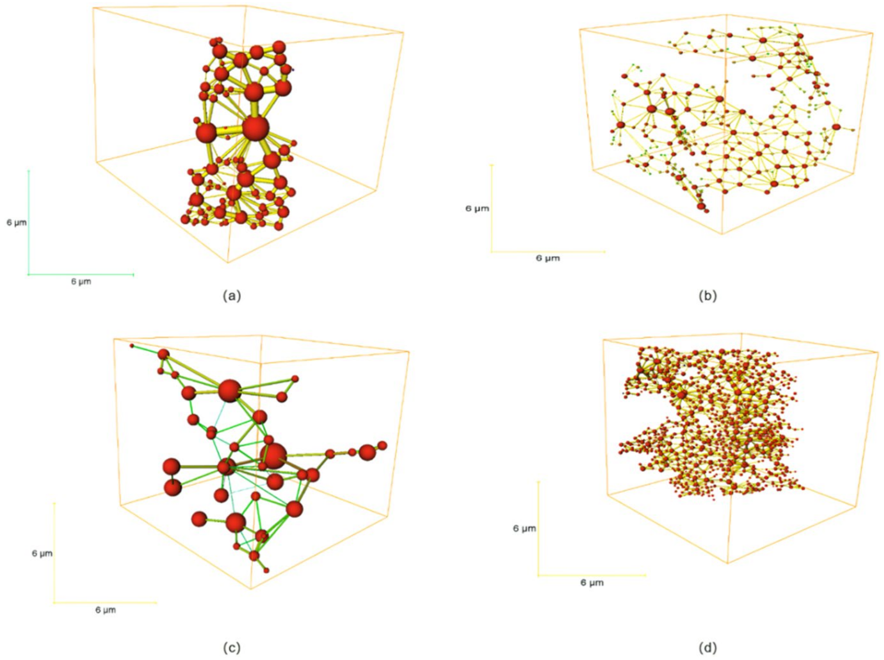

Fig. 23. Microscopic pore–throat structure distribution of fracture bodies: (**a**–**d**) show schematic diagrams of the microscopic pore–throat structures of fractures in CS1, W21, CS105, and DS9, respectively. Red spheres represent pores, and yellow connecting tubes represent throats.

Parameter	CS1 Fractures	W21 Fracture	CS105 Fractures	DS9 Fractures
Total pore volume (μm^3)	7.37	7.38	24.87	10.48
Total pore surface area (μm^2)	171.36	352.35	2501.27	454.36
Average pore volume (μm^3)	0.091	0.03	0.67	0.013
Average pore surface area (μm^2)	2.12	1.43	67.6	0.58
Total throat volume (μm^2)	12.70	5.42	3.24	9.46
Average throat volume (μm^2)	0.067	0.012	0.048	0.0065
Total throat length (μm)	177.58	424.48	160.56	663.62
Average throat length (μm)	0.93	0.90	2.36	0.45
Average throat radius (μm)	0.13	0.064	0.11	0.052
Average pore radius (μm)	0.22	0.17	0.44	0.13
Number of pores	81	246	37	777
Number of throats	189	471	68	1463
Maximum coordinated number	18	12	9	11
Average coordinated number	4.7	3.82	3.68	3.77

Table 5. Pore–throat parameters. Note: CS1 denotes a rhyolitic crystal–lithic tuff; W21 denotes a dacitic crystal–lithic tuff; CS105 denotes a volcanic tuff; DS9 denotes a porphyritic andesite.

Fracture-network structural characteristics

At the micrometer scale, the fracture dissolution model (Fig. 24) shows that the CS1 fracture network nearly cuts vertically through the entire rock sample, forming axially throughgoing pathways with well-developed and densely distributed dissolution tracks. In contrast, the W21 fracture structure is fragmented, with short and dispersed internal dissolution paths that struggle to form continuous migration channels for natural gas. In the other sample set, the CS105 fractures exhibit strong spatial extensibility, with pathway branches forming in some locations that favor the development of continuous gas-transport routes. By comparison, the DS9 fractures are irregular in shape, have unstable orientations, and show weak propagation capability. Therefore, from the perspective of microscopic dissolution characteristics, the CS1 and CS105 fractures enhance reservoir connectivity and promote dynamic transport of natural gas.

Considering that under the same structural stress, rhyolite, an acidic rock, is more brittle and prone to high-density fracturing compared to andesite; tuff, on the other hand, is more plastic and has fewer fractures. The single segments analysis can't perfectly show the connectivity in all of those samples.

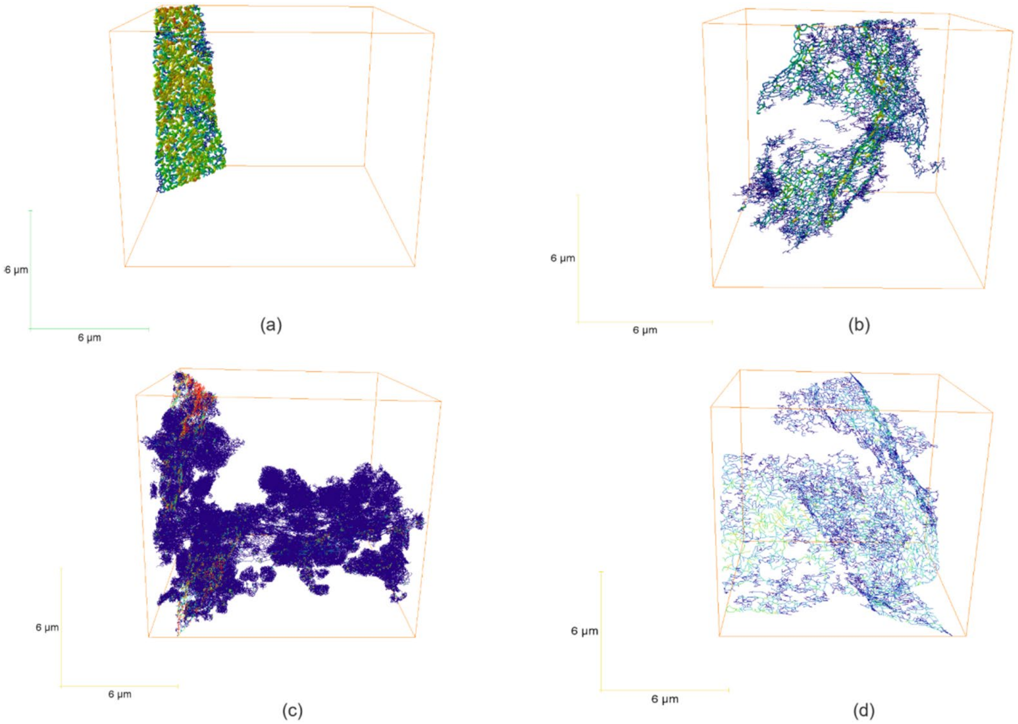

Fig. 24. 3D distribution of fracture dissolution models: (**a**–**d**) schematic diagrams of the 3D fracture dissolution models for CS1, W21, CS105, and DS9, respectively.

Parameter	CS1 fractures	W21 fractures	CS105 fractures	DS9 fractures
Average thickness (μm)	0.041	0.017	0.00069	0.019
Biggest thickness (μm)	0.087	0.048	0.034	0.086
Nodes	2179	7958	153,768	14,175
Segments	2177	11,074	322,552	125,944

Table 6. Parameters of dissolution fractures. Note: CS1 denotes a rhyolitic crystal–lithic tuff; W21 denotes a dacitic crystal–lithic tuff; CS105 denotes a volcanic tuff; DS9 denotes a porphyritic andesite.

Quantitative results (Table 6) indicate that the CS1 fracture network has larger average and maximum apertures, reducing resistance during natural-gas migration and thereby improving the reservoir's effective permeability. In the other sample set, the CS105 fractures, owing to a richer internal dissolution network, construct densely connected lateral micro-channels for gas migration, efficiently facilitating effective transport of natural gas. Taken together, both qualitative and quantitative analyzes demonstrate that CS1 and CS105 fractures have clear advantages in promoting natural-gas migration.

Gas flow paths and permeability analysis

Figure 25 presents a natural-gas percolation simulation based on Darcy's law[39]. In CS1, the streamlines are continuous and dense overall; they spread rapidly inward from the fracture inlet to the outlet, showing a clear radial pattern. The seepage paths extend along the fracture network and traverse the entire simulation domain, indicating strong overall connectivity and conveyance capacity. In contrast, W21 exhibits markedly fewer streamlines with a scattered, discontinuous distribution; the fluid achieves only short-distance penetration in local areas and fails to establish a complete, continuous percolation pathway. Quantitatively, the permeability of CS1 is 0.109 mD, and the flow rate is 7.66×10^6 μm³/s, which are 4.5 and 5.1× those of W21 (0.024 mD and 1.51×10^6 μm³/s), respectively. In summary, CS1 not only has higher natural-gas permeability but also provides superior internal transport pathways within its fracture network, thereby enhancing the efficiency of natural-gas transport, whereas W21 is constrained by fracture discontinuity, with broken migration paths and weaker transport capacity, resulting in a markedly reduced reservoir response. This further verifies that, under high porosity–permeability conditions, the internal fracture network can promote efficient natural-gas migration by establishing complete, continuous seepage channels.

In the other sample set, fractures in CS105 form multiple uniformly distributed, highly connected high-efficiency channels, exhibiting an overall throughgoing structure from inlet to outlet along the depth direction. The seepage rate and permeability of CS105 are 7.78×10^6 μm³/s and 0.202 mD, respectively, far exceeding those

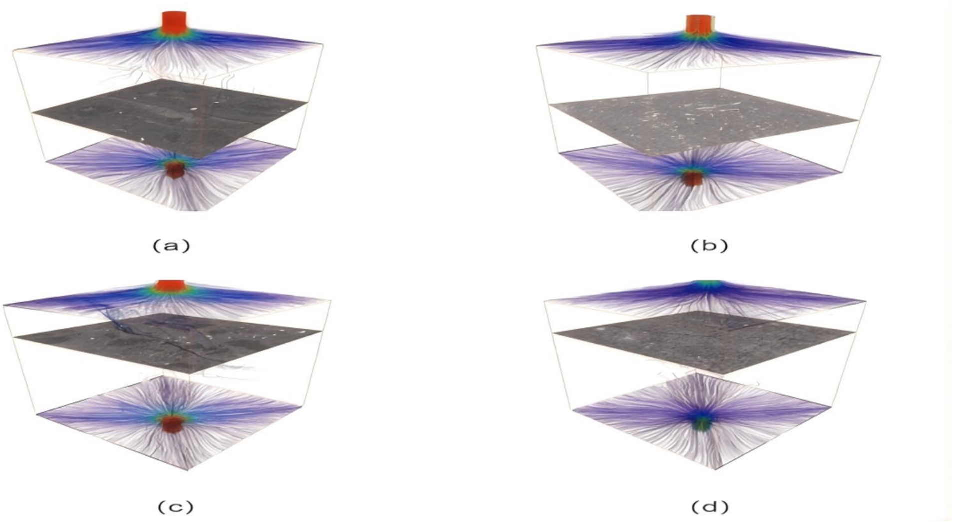

Fig. 25. 3D natural-gas percolation simulation results, where (**a**) corresponds to CS105, (**b**) to W21, (**c**) to CS105, and (**d**) to DS9.

of DS9 (4.81×10^5 μm³/s and 1.11×10^{-5} mD). The experimental results indicate that the highly connected fracture network within CS105 greatly enhances the efficiency of natural-gas migration, further confirming that under low porosity–permeability conditions, the fracture network plays a dominant role in improving natural-gas transport capacity.

Discussions

Comparative analysis of fracture-segmentation methods

Due to the pronounced heterogeneity of volcanic reservoirs and the coupling effects of CT scanning and imaging, traditional segmentation methods—such as Otsu's method and simple thresholding—struggle to achieve precise segmentation of micro-fractures[38,40]. However, manually annotating every slice to train machine-learning or deep-learning models is highly labor- and time-consuming[41]. Therefore, in this study we combine traditional segmentation with manual annotation: after preprocessing the slices by thresholding, we use a brush tool to refine the results, thereby obtaining reasonably satisfactory fracture segmentations in a shorter time for subsequent machine-learning training.

Experimental results show that a 2D ensemble-learning model can achieve fast and effective segmentation of volcanic-rock fractures, but some pores are still retained in the images, which is unfavorable for further investigating the impact of fracture networks on natural-gas percolation. However, directly using 2.5D or 3D deep-learning models for fracture segmentation not only greatly increases training difficulty and time, but also heightens reliance on computing performance[42]. Therefore, by first applying a 2D ensemble-learning model for pre-segmentation of micro-pores and fractures and then using a 2.5D U-Net + + model for complete fracture segmentation, accurate segmentation of volcanic-rock fractures can be achieved within a shorter training time.

However, when computing hardware is adequate and time is sufficient, Chen[10] directly used a 3D deep-learning model and obtained satisfactory fracture-segmentation results. Therefore, selecting an appropriate model to achieve precise fracture segmentation under different research conditions remains a key issue for future geoscience research.

Fracture-network regulation of natural-gas migration under multi-scale parameter synergy

Results of basic petrophysical analysis (Table 7) indicate that, in tight volcanic reservoirs, the multi-scale parameters of the fracture network jointly influence the initial storage and migration capacity of natural gas[43]. In the high-efficiency reservoir samples CS1 and CS105, the internal fracture networks exhibit large volumes, strong connectivity, and structural integrity across scales; their pore–throat architectures show wide conduit characteristics that effectively promote rapid gas movement and efficient production. By contrast, in the low-efficiency samples W21 and DS9, the fracture networks are fragmented and discontinuous, with slender throats that are often isolated branches, making it difficult to construct diverse, hierarchically throughgoing flow pathways; consequently, although DS9 has higher porosity, its gas-diffusion efficiency is far lower than that of CS105. Comparative analysis of the two sample sets shows that the fracture network, through its multi-scale parameters, jointly governs the efficiency of natural-gas migration, and single porosity–permeability metrics alone are insufficient to represent effective transport capacity.

However, it is noted that although the PNM model has greatly shown the connectivity from different samples, we acknowledge that fractal analysis has unique advantages in describing the cross-scale evolution of fractures. Volcanic rock fractures typically exhibit multi-scale distribution characteristics, and introducing fractal dimensions will help establish an up-scaling model from micrometer-level μCT images to centimeter-scale core

Parameter	CS1 Fractures	W21 Fractures	CS105 Fractures	DS9 Fractures
Average throat radius (μm)	0.13	0.064	0.11	0.052
Biggest throat length (μm)	0.93	0.90	2.36	0.45
Average coordination number	4.7	3.82	3.68	3.77
Average pore radius (μm)	0.22	0.17	0.44	0.13
Permeability (mD)	0.109	0.024	0.202	0.000011
Porosity (%)	12.6	5.4	2.3	3.3

Table 7. Parameters and simulation. Note: CS1 denotes a rhyolitic crystal–lithic tuff; W21 denotes a dacitic crystal–lithic tuff; CS105 denotes a volcanic tuff; DS9 denotes a porphyritic andesite.

samples. This is considered an important direction for our future research, aiming to further reveal the evolution patterns of fracture networks under stress through fractal dynamics.

Analysis of the dominant effect of fracture networks on the evolution of natural-gas seepage

The 3D distribution models and skeletonized models jointly demonstrate that the geometry and connectivity of the fracture network are key factors determining the efficiency of natural-gas seepage. In volcanic samples CS1 and CS105, axially throughgoing master fractures not only provide preferential migration pathways, but—via diverse internal dissolution channels—also laterally connect pore spaces within the rock, acting in concert with the surrounding matrix to further enhance overall gas permeability. By contrast, in samples W21 and DS9, structurally fragmented and isolated fractures fail, at the macroscale, to provide longitudinally throughgoing transport paths for gas, and, at the microscale, to form lateral dissolution–drainage systems, which markedly weakens the continuity of fluid migration and limits the effective transport of natural gas.

Seepage simulation results (Fig. 26) show that the fracture network exerts a primary control on the evolution of natural-gas seepage and directly affects effective migration. In volcanic samples CS1 and CS105 with large apertures and well-developed fractures, natural gas enters at the fracture inlet, migrates directionally along the fracture trend, and exits smoothly at the outlet. Secondary streamlines radiate into the surrounding rock matrix and merge with the main fracture conduit at the outlet, efficiently enhancing gas permeability and flow rate. In contrast, in samples W21 and DS9 with small apertures and fragmented fractures, fragmentation of the main internal channels and isolation as well as dispersion of secondary transport paths cause a marked decay of gas velocity in the fracture midsections, with local interruptions of streamlines. This prevents the formation of a complete throughgoing flow field and hinders the effective migration of natural gas.

It should be noted that the seepage simulations in this study were conducted solely on the basis of classical Darcy's law, without incorporating parameters such as fracture aperture, stress, and temperature; therefore, the precise effects of individual fracture metrics on natural-gas migration cannot be determined[44,45].

Firstly, the digital core model constructed in this paper is based on the CT image at normal temperature and pressure in the laboratory. In actual strata, when rocks are in a high effective stress environment, fractures tend to close or nonlinear deformation, resulting in a significant decrease in permeability. Secondly, thermal effects can not be ignored in volcanic reservoirs, and thermal stress may induce new micro-fractures or change the connectivity of existing pore throats[46]. In addition, the fracture opening (aperture) is simplified in the calculation, and the spatial heterogeneity along the fracture plane is not fully considered. Consequently, future research should explicitly incorporate fracture parameters and employ multiple methods to investigate their impacts on natural-gas seepage simulations.

Secondly, mineral alteration (especially the kaolinization of feldspar) would be another key factor on fracture permeability. To begin with, there is physical clogging, which directly reduces the effective aperture. Then, clay minerals increase the microscopic roughness of fracture surfaces, significantly enhancing the frictional resistance to fluid flow. Hence, mineral alteration should be the key to studying fracture permeability in the next step. And also, "the integration of nanomaterials presents a transformative approach to modulating the apparent viscosity of heavy oil through catalytic aquathermolysis and asphaltene dispersion. However, a rigorous environmental impact assessment (EIA) is imperative[47]. Future studies should prioritize the synergistic effects of nanoparticle transport on reservoir integrity and the long-term ecotoxicological footprint of residual particles within the subsurface environment".

On the same time, although this study evaluates intrinsic permeability based on Darcy's law, in actual tight reservoirs, non-Darcy effects should be considered. For example, when the pressure gradient is high, fluid flow in wide fractures exhibits inertial resistance, following the Forchheimer equation:

$$-\forall P = \frac{\mu}{\mathrm{k}} v + \beta \rho v^2 \tag{4}$$

Here, β is the non-Darcy coefficient. In addition, considering the compressibility of the gas and the slip effect (Klinkenberg effect), a correction factor needs to be introduced in subsequent dynamic recovery simulations to adjust the permeability predictions under low-pressure conditions. This transition from a 'static geometric topology' to 'dynamic multi-mechanism flow' should be put into consideration for further study.

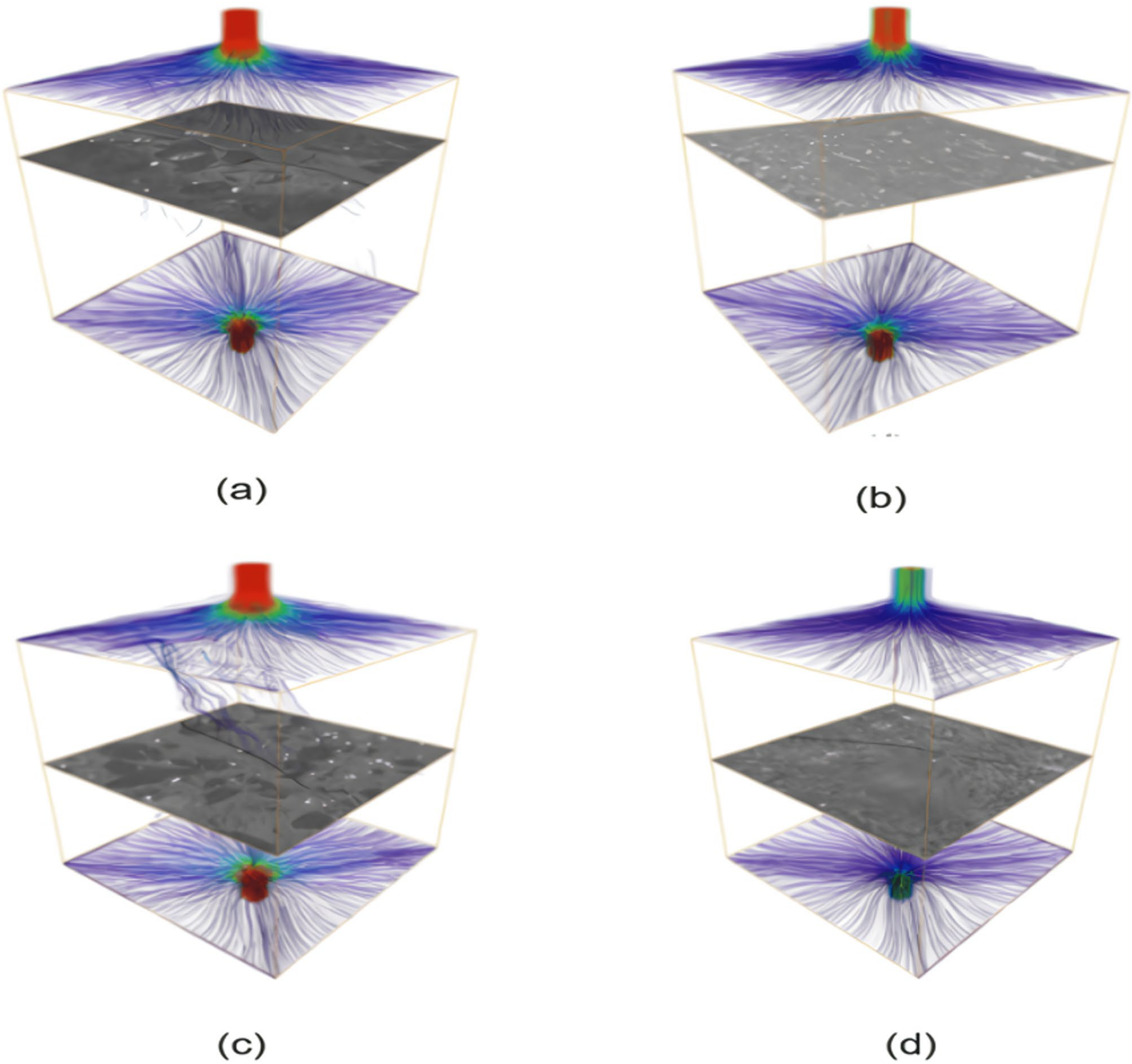

Fig. 26. Schematic of 3D natural-gas seepage simulation results: (**a**–**d**) correspond to the simulations for samples CS1, W21, CS105, and DS9, respectively. In CS1, streamlines traverse the entire rock from top to bottom along the fracture network; in W21, streamlines break in the middle of the rock and fail to form an effective seepage pathway; in CS105, streamlines are dense and diverse, axially connecting the entire seepage channel; whereas in DS9, streamlines are sparse and isolated.

Conclusions

Using CT scanning, ensemble learning, and deep learning, we quantitatively and visually analyzed the connectivity and spatial characteristics of fracture networks in volcanic rocks. We also investigated how fracture networks affect natural-gas seepage under both high- and low-porosity–permeability conditions. The main conclusions are as follows:

1. We propose an automatic segmentation method for volcanic micro-fractures that progresses from a 2D ensemble-learning model to a 2.5D deep-learning model, employing a semi-automatic "label-as-you-train" strategy to balance timeliness under hardware constraints. Experimental results show that the method achieved a Dice coefficient of 0.902 in only 10 epochs.
2. We establish an integrated evaluation system of "segmentation–visual modeling–petrophysical quantitative analysis–seepage simulation". Visual modeling and quantitative analysis based on fracture segmentation indicate that high-efficiency reservoirs (CS1, CS105) exhibit multi-parameter advantages, such as larger fracture volumes and greater pore–throat radii—which significantly enhance the efficiency of natural-gas

migration. Gas seepage simulations show that the fracture network governs the entire process of natural-gas storage and migration within the flow field and markedly affects seepage efficiency.

3. In summary, a well-developed fracture network serves as the principal seepage pathway in volcanic reservoirs, significantly enhancing internal connectivity and enabling efficient gas migration even under tight, low-porosity–permeability conditions. Overall, the main channels of the fracture network govern the bulk effective permeability and transport efficiency, whereas lateral micro-channels determine the upper limit of gas transport.
4. Although this study provides a three-tier coupled evaluation framework linking "segmentation accuracy–topological connectivity–transport capacity", it still has some limitations. First, constrained by CT scanning resolution and insufficient algorithmic accuracy, it may be inadequate to detect the entire fracture network. Second, it should be noted that the quantitative parameters reported in this study, such as pore/fracture volume, were obtained at micron-level. Due to the trade-off between resolution and field of view (FOV) in CT imaging, the scale of analysis fails to cover the macroscopic heterogeneity of the entire core. However, this study mainly focuses on the topological reconstruction and algorithm validation of micro-fractures, and the current sampling volume has included representative microstructural features at this scale. Future work will further evaluate the evolution of representative fundamental volume (REV) from micron to centimeter scale across scales through multiscale fusion imaging techniques to achieve more comprehensive reservoir characterization. Third, in the seepage analysis, we did not construct an integrated evaluation system of "flow field–flow velocity–heat transfer". Given the heterogeneity in surface wettability caused by mineral alteration, upcoming work will incorporate multiphase flow simulations to quantify the impact of clay minerals on relative permeability curves and capillary pressure, providing a more comprehensive physical framework for multi-scale reservoir assessment. Future research should focus on introducing stress sensitivity models and thermal parameters to explore the evolution patterns of microscopic topologies under multi-field coupling conditions and incorporate broader geological conditions and adopt multiple methods to verify and extend these conclusions.

Data availability

The data presented in this study are available on request from the corresponding author. The data are not publicly available due to being collected and sorted by authors from some paid databases.

Received: 6 January 2026; Accepted: 6 February 2026

References

1. Tao, S. Exploration and development of unconventional oil and gas resources: latest advances and prospects. *Energies* **18**, 3933. https://doi.org/10.3390/en18153933 (2025).
2. Zhang, N. et al. Fracture conductivity and rock appearance in volcanic reservoirs treated by various stimulation techniques. *Energy* **295**, 131045. https://doi.org/10.1016/j.energy.2024.131045 (2024).
3. Liao, Q. et al. Reservoir stimulation for unconventional oil and gas resources: recent advances and future perspectives. *Adv. Geo-Energy Res.* **13**, 7–9. https://doi.org/10.46690/ager.2024.07.02 (2024).
4. Li, Y. et al. Quantitative prediction of fracture parameters in volcanic reservoirs using integrated rock physics and BO-BiLSTM network approach. *IEEE Trans. Geosci. Remote Sens.* **63**, 1–14. https://doi.org/10.1109/TGRS.2025.3581090 (2025).
5. Tahir, M. U. & Guo, S. Preliminary investigation of fracture behavior during carbon dioxide fracturing of natural hydrogen reservoir with Hard-Core imperfections. *Reserv. Sci.* **2**, 34–51. https://doi.org/10.62762/RS.2025.759326 (2026).
6. Gao, X. et al. Micro–nano 3D CT scanning to assess the impact of microparameters of volcanic reservoirs on gas migration. *Processes* **12**, 2000. https://doi.org/10.3390/pr12092000 (2024).
7. Da Silva, L. C. V. et al. Entropy-based measure of rock sample heterogeneity derived from micro-CT images. *Transp. Porous Media.* **152**, 44. https://doi.org/10.1007/s11242-025-02183-3 (2025).
8. Lee, D. et al. Detecting micro fractures: A comprehensive comparison of conventional and machine-learning-based segmentation methods. *Solid Earth.* **13**, 1475–1494. https://doi.org/10.5194/se-13-1475-2022 (2022).
9. Zhang, L. et al. The characterization of bituminous coal microstructure and permeability by liquid nitrogen fracturing based on μCT technology. *Fuel* **262**, 116635. https://doi.org/10.1016/j.fuel.2019.116635 (2020).
10. Chen, S. et al. Evolution of coal microfracture by Cyclic fracturing of liquid nitrogen based on μCT and convolutional neural networks. *Rock. Mech. Rock. Eng.* **57**, 2103–2124. https://doi.org/10.1007/s00603-023-03649-w (2024).
11. Xu, J. et al. Basin evolution and oil shale deposition during upper cretaceous in the Songliao basin (NE China): implications from sequence stratigraphy and geochemistry. *Int. J. Coal Geol.* **149**, 9–23. https://doi.org/10.1016/j.coal.2015.07.005 (2015).
12. Chi, H. et al. Geophysical characteristics of internal weathered volcanic crust in the Songliao basin. *Acta Geophys.* **73**, 221–233. https://doi.org/10.1007/s11600-024-01356-w (2024).
13. Wu, H. C. et al. Integrated chronostratigraphic framework for cretaceous strata in the Songliao basin. *Earth Sci. Front.* **31**, 431–445. https://doi.org/10.13745/j.esf.sf.2024.1.22 (2024).
14. Meng, S-W. et al. Mechanical characteristics and reservoir stimulation mechanisms of the Gulong shale oil reservoirs, the Northern Songliao basin. *Pet. Sci.* **21**, 2023–2036. https://doi.org/10.1016/j.petsci.2023.11.002 (2024).
15. Liu, Y-K. et al. Rare Earth elemental and Sr isotopic evidence for seawater intrusion event of the Songliao basin 91 million years ago. *Pet. Sci.* **20**, 1347–1362. https://doi.org/10.1016/j.petsci.2022.11.015 (2023).
16. Zhu, J. et al. Multi-scale CT imaging technique characterization of volcanic rock reservoirs: A study case from the Changling fault depression of the Southern Songliao basin. *Front. Earth Sci.* **13**, 1456257. https://doi.org/10.3389/feart.2025.1456257 (2025).
17. Sun, Y. et al. Structural characteristics of faults in Wangfu fault depression and their control on coal-rock gas enrichment, Songliao Basin, NE China. *Pet. Explor. Dev.* **52**, 649–662. https://doi.org/10.1016/S1876-3804(25)60594-5 (2025).
18. Liu, L. et al. The relationship between physical property evolution and reservoir formation in volcanic rock reservoirs: the huoshiling Formation, Dehui fault Depression, Southern Songliao basin. *Mar. Pet. Geol.* **179**, 107446. https://doi.org/10.1016/j.marpetgeo.2025.107446 (2025).
19. Wang, T. et al. High-precision geochronology of the early cretaceous Yingcheng formation and its stratigraphic implications for Songliao Basin, China. *Geosci. Front.* **13**, 101386. https://doi.org/10.1016/j.gsf.2022.101386 (2022).
20. Withers, P. J. et al. X-ray computed tomography. *Nat. Rev. Methods Primer.* **1**, 18. https://doi.org/10.1038/s43586-021-00015-4 (2021).

21. Miyazaki, T. et al. Measurement of the particle density of small amounts of pharmaceutical powders using high-contrast micro X-ray computed tomography. *Powder Technol.* **457**, 120929. https://doi.org/10.1016/j.powtec.2025.120929 (2025).
22. Wu, H. et al. Imaged based fractal characterization of micro-fracture structure in coal. *Fuel* **239**, 53–62. https://doi.org/10.1016/j.fuel.2018.10.117 (2019).
23. Fan, Y. et al. Reconstructing data representation for multi-label feature selection. *Pattern Recognit.* **169**, 111941. https://doi.org/10.1016/j.patcog.2025.111941 (2026).
24. Jin, C. et al. Segmentation of ore and waste rocks in borehole images using the multi-module densely connected U-net. *Comput. Geosci.* **159**, 105018. https://doi.org/10.1016/j.cageo.2021.105018 (2022).
25. Shaker, M. H. & Hüllermeier, E. Random forest calibration. *Knowl-Based Syst.* **328**, 114143. https://doi.org/10.1016/j.knosys.2025.114143 (2025).
26. He, C. et al. 3D analysis of mineralogical and fracture features in granite and impact of biotite distribution on uniaxial compressive strength. *Eng. Geol.* **356**, 108279. https://doi.org/10.1016/j.enggeo.2025.108279 (2025).
27. Xing, S. et al. 2.5D-UNet-HC: 2.5D-UNet based on hybrid Convolution for prostate ultrasound image segmentation. *IEEE Access.* **13**, 178652–178662. https://doi.org/10.1109/ACCESS.2025.3620348 (2025).
28. Singh, A. et al. On representative elementary volumes of grayscale micro-CT images of porous media. *Geophys. Res. Lett.* **47**, e2020GL088594. https://doi.org/10.1029/2020GL088594 (2020).
29. Zhang, P. et al. Unet-based image segmentation and binarization for water level detection. *Vis. Comput.* **41**, 7367–7377. https://doi.org/10.1007/s00371-025-03810-2 (2025).
30. Wei, S. et al. Classification of ground information during wildfires: using an improved UNet model. *Int. J. Disaster Risk Reduct.* **116**, 105157. https://doi.org/10.1016/j.ijdrr.2024.105157 (2025).
31. Hou, Z. et al. UAV target segmentation based on depse Unet + + modeling. *Drones* **9**, 166. https://doi.org/10.3390/drones9030166 (2025).
32. Angermann, C. & Haltmeier, M. Random 2.5D U-net for fully 3D segmentation. In: (eds Liao, H., Balocco, S., Wang, G., Zhang, F., Liu, Y., Ding, Z. et al.) Mach. Learn. Med. Eng. Cardiovasc. Health Intravasc. Imaging Comput. Assist. Stenting, Shenzhen, China: Springer International Publishing; 158–166. https://doi.org/10.1007/978-3-030-33327-0_19. (2019).
33. Zhou, Z. et al. UNet++: A nested U-Net architecture for medical image segmentation. In: (eds Stoyanov, D., Taylor, Z., Carneiro, G., Syeda-Mahmood, T., Martel, A. & Maier-Hein, L.) Deep Learn. Med. Image Anal. Multimodal Learn. Clin. Decis. Support, Granada, Spain: Springer International Publishing; 3–11. https://doi.org/10.1007/978-3-030-00889-5_1. (2018).
34. Tan, K. J. et al. Research on effectiveness of effective pore aspect ratio based on pore-throat characteristics of digital core. *Chin. J. Geophys.* **65**, 4433–4447. https://doi.org/10.6038/cjg2022P0393 (2022).
35. Zhao, X. et al. Modeling of permeability and formation factor of carbonate digital rocks: Dual-pore-network and pore-network-continuum models. *Transp. Porous Media.* **152**, 37. https://doi.org/10.1007/s11242-025-02177-1 (2025).
36. Bataineh, B. An iterative thinning algorithm for binary images based on sequential and parallel approaches. *Pattern Recognit. Image Anal.* **28**, 34–43. https://doi.org/10.1134/S1054661818010030 (2018).
37. Alcántara-López, F. et al. Spatial fractional darcy's law on the diffusion equation with a fractional time derivative in Single-Porosity naturally fractured reservoirs. *Energies* **15**, 4837. https://doi.org/10.3390/en15134837 (2022).
38. Zhang, H. et al. Pore-scale characterization and PNM simulations of multiphase flow in carbonate rocks. *Energies* **14**, 6897. https://doi.org/10.3390/en14216897 (2021).
39. Keogh, R. R. et al. Active darcy's law. *Phys. Rev. Lett.* **132**, 188301. https://doi.org/10.1103/PhysRevLett.132.188301 (2024).
40. Liu, Y. et al. Quantitative characterization of tight rock microstructure of digital core. *Geofluids* **2022**, 1–18. https://doi.org/10.1155/2022/3554563 (2022).
41. Ge, L. et al. Label correlation for partial label learning. *J. Syst. Eng. Electron.* **33**, 1043–1051. https://doi.org/10.23919/JSEE.2022.000102 (2022).
42. Zhang, G. et al. Automatic lung tumor segmentation from CT images using improved 3D densely connected UNet. *Med. Biol. Eng. Comput.* **60**, 3311–3323. https://doi.org/10.1007/s11517-022-02667-0 (2022).
43. Song, M. S. et al. Study on the fracture distribution pattern of volcanicrock in thrust fault developed zone. *Nat. Gas Geosci.* **28**, 989–999. https://doi.org/10.11764/j.issn.1672-1926.2017.06.011 (2017).
44. Bao, D. et al. Pore structure and seepage characteristics of hydrate-bearing sediments. *Energy Fuels.* **39**, 3087–3096. https://doi.org/10.1021/acs.energyfuels.4c05720 (2025).
45. Wang, C. Y. Fluid seepage into a rotating channel filled with a porous medium. *J. Eng. Mech.* **151**, 4024107. https://doi.org/10.1061/JENMDT.EMENG-8037 (2025).
46. Li, W. & Liao, J. Microscopic analysis of flow resistance of oil displacement fluid in reservoir fractures. *Reserv. Sci.* **2**, 16–33. https://doi.org/10.62762/RS.2025.837826 (2026).
47. Xu, N. & Wang, Y. Effect of nanomaterials on improving the apparent viscosity of heavy oil and the environmental evaluation of reservoir environment. *Reserv. Sci.* **2**, 1–15. https://doi.org/10.62762/RS.2025.277961 (2026).

Acknowledgements

We thank Sanying Precision Instruments Co., Ltd. for the technical support and equipment provided for this research. We appreciate the assistance of the Exploration and Development Research Institute of Jilin Oilfield Branch, China National Petroleum Corporation (CNPC), for sample preparation., and are grateful for their support.

Author contributions

Conceptualization, Jiacheng Zhang and Yunliang Yu; methodology, Jiacheng Zhang; software, Jiacheng Zhang; validation, formal analysis, Jiacheng Zhang and Yunliang Yu; investigation, Jiacheng Zhang; resources, Yunliang Yu; data curation, Yunliang Yu; writing—original draft preparation, Jiacheng Zhang; writing—review and editing, Jiacheng Zhang, Yunliang Yu, Hongchen Cai and Mengyu Li; visualization, Jiacheng Zhang; supervision, Yunliang Yu and Yingchun Liu; project administration, Yunliang Yu; funding acquisition, Yunliang Yu. All authors have read and agreed to the published version of the manuscript.

Funding

This research was funded by the National Natural Science Foundation of China (No. 41472101).

Declarations

Competing interests

The authors declare no competing interests.

Additional information

Correspondence and requests for materials should be addressed to Y.Y.

Reprints and permissions information is available at www.nature.com/reprints.

Publisher's note Springer Nature remains neutral with regard to jurisdictional claims in published maps and institutional affiliations.

Open Access This article is licensed under a Creative Commons Attribution-NonCommercial-NoDerivatives 4.0 International License, which permits any non-commercial use, sharing, distribution and reproduction in any medium or format, as long as you give appropriate credit to the original author(s) and the source, provide a link to the Creative Commons licence, and indicate if you modified the licensed material. You do not have permission under this licence to share adapted material derived from this article or parts of it. The images or other third party material in this article are included in the article's Creative Commons licence, unless indicated otherwise in a credit line to the material. If material is not included in the article's Creative Commons licence and your intended use is not permitted by statutory regulation or exceeds the permitted use, you will need to obtain permission directly from the copyright holder. To view a copy of this licence, visit http://creativecommons.org/licenses/by-nc-nd/4.0/.

© The Author(s) 2026